The wind speeds, dust content, and mass-loss rates of evolved AGB and RSG stars at varying metallicity

Steven R. Goldman,[1][*] Jacco Th. van Loon,[1] Albert A. Zijlstra,[2] James A. Green,[3,4] Peter R. Wood,[5] Ambra Nanni,[6] Hiroshi Imai,[7] Patricia A. Whitelock,[8,9] Mikako Matsuura,[10] Martin A. T. Groenewegen[11] and José F. Gómez[12]

[1]*Astrophysics Group, Lennard–Jones Laboratories, Keele University, Staffordshire ST5 5BG, UK*
[2]*Jodrell Bank Centre for Astrophysics, Alan Turing Building, School of Physics and Astronomy, The University of Manchester, Oxford Road, Manchester M13 9PL, UK*
[3]*SKA Organisation, Jodrell Bank Observatory, Lower Withington, Macclesfield, Cheshire SK11 9DL, UK*
[4]*CSIRO Astronomy and Space Science, Australia Telescope National Facility, PO Box 76, Epping, NSW 1710, Australia*
[5]*Research School of Astronomy and Astrophysics, Australian National University, Weston Creek, ACT 2611, Australia*
[6]*Dipartimento di Fisica e Astronomia Galileo Galilei, vicolo dell'Osservatorio 3, I-35141 Padova PD, Italy*
[7]*Department of Physics and Astronomy, Kagoshima University, 1-21-35 Korimoto, Kagoshima 890-0065, Japan*
[8]*South African Astronomical Observatory (SAAO), PO Box 9, 7935 Observatory, South Africa*
[9]*Astronomy Department, University of Cape Town, 7701 Rondebosch, South Africa*
[10]*School of Physics and Astronomy, Cardiff University, Queen's Buildings, The Parade, Cardiff CF24 3AA, UK*
[11]*Royal Observatory of Belgium, Ringlaan 3, B-1180 Brussels, Belgium*
[12]*Instituto de Astrofísica de Andalucía, CSIC, Glorieta de la Astronomía s/n, E-18008 Granada, Spain*

ABSTRACT

We present the results of our survey of 1612-MHz circumstellar OH maser emission from asymptotic giant branch (AGB) stars and red supergiants (RSGs) in the Large Magellanic Cloud (LMC). We have discovered four new circumstellar maser sources in the LMC, and increased the number of reliable wind speeds from infrared (IR) stars in the LMC from 5 to 13. Using our new wind speeds, as well as those from Galactic sources, we have derived an updated relation for dust-driven winds: $v_{exp} \propto ZL^{0.4}$. We compare the subsolar metallicity LMC OH/IR stars with carefully selected samples of more metal-rich OH/IR stars, also at known distances, in the Galactic Centre and Galactic bulge. We derive pulsation periods for eight of the bulge stars for the first time by using near-IR photometry from the Vista Variables in the Via Lactea survey. We have modelled our LMC OH/IR stars and developed an empirical method of deriving gas-to-dust ratios and mass-loss rates by scaling the models to the results from maser profiles. We have done this also for samples in the Galactic Centre and bulge and derived a new mass-loss prescription which includes luminosity, pulsation period, and gas-to-dust ratio $\dot{M} = 1.06^{+3.5}_{-0.8} \times 10^{-5}(L/10^4 \, \mathrm{L_\odot})^{0.9\pm0.1}(P/500 \, \mathrm{d})^{0.75\pm0.3}(r_{gd}/200)^{-0.03\pm0.07} \, \mathrm{M_\odot \, yr^{-1}}$. The tightest correlation is found between mass-loss rate and luminosity. We find that the gas-to-dust ratio has little effect on the mass-loss of oxygen-rich AGB stars and RSGs within the Galaxy and the LMC. This suggests that the mass-loss of oxygen-rich AGB stars and RSGs is (nearly) independent of metallicity between a half and twice solar.

Key words: masers – stars: AGB and post-AGB – stars: mass-loss – supergiants – stars: winds, outflows – Magellanic Clouds.

1 INTRODUCTION

A remarkable aspect of the evolution of asymptotic giant branch (AGB) stars ($0.8 \lesssim M \lesssim 8 \, \mathrm{M_\odot}$) and some red supergiants (RSGs)

($M \lesssim 8 \, \mathrm{M_\odot}$) is their period of intense mass-loss. Near the end of their lifetime, AGB stars will lose up to 85 per cent of their initial mass at a rate of up to $10^{-4} \, \mathrm{M_\odot \, yr^{-1}}$, and contribute a significant amount of dust and chemically enriched material to the interstellar medium (ISM) (Herwig 2005). They may collectively contribute more dust to the ISM than any other type of celestial body in the Universe. Yet, this is still controversial, as the effects of

[*] E-mail: s.r.goldman@keele.ac.uk

metallicity and luminosity on the mass-loss of these stars remain unclear. Massive AGB stars and RSGs have been instrumental in the ongoing star formation and chemical evolution of massive spheroidals at high redshift, and possibly in the multiple populations found in massive Galactic globular clusters. Constraining this mass-loss rate is also highly important for understanding supernova progenitors and light curves. Mass-loss models have been developed and refined (Reimers 1975; Baud & Habing 1983; Schröder & Cuntz 2005; van Loon, Marshall & Zijlstra 2005) but require observations for verification.

During their stage of intense mass-loss, AGB and RSG stars lose mass in the form of a stellar 'superwind', a concept first introduced by Iben & Renzini (1983). This superwind is accelerated by radiation pressure on circumstellar dust grains and produces velocities ranging from about 5 to 30 km s^{-1}. The dust grains form at a few stellar radii and are composed of either carbonaceous or silicate dust grains, depending on the composition of the star's atmosphere and the efficiency of hot-bottom burning and third dredge-up events (Herwig 2005). Stars with an initial mass $\lesssim 1.5\,M_\odot$ or $\gtrsim 4\,M_\odot$ and metallicity within a factor of few around solar will end their lives oxygen-rich.

The large quantity of dust surrounding some of these stars leaves many of them obscured at visual wavelengths. However, the stellar light heats dust grains, which re-emit energy in the infrared (IR). By modelling the spectral energy distributions (SEDs) and making assumptions, we can derive important and hard-to-obtain stellar parameters such as stellar mass-loss rate and wind speed. Dusty oxygen-rich AGB and RSG stars often also exhibit OH, H_2O, and SiO maser emission (Nyman, Hall & Olofsson 1998). From these unique properties, these stars have been aptly named OH/IR stars.

OH/IR stars generally emit their strongest OH masers at 1612 MHz, which occurs at several hundred stellar radii from the star. These masers are pumped by IR radiation and trace terminal velocities of the envelope's expansion due to their large distances from the central star (Elitzur 1992). The OH molecules are formed when H_2O molecules at the periphery of the inner envelope are photodissociated by interstellar ultraviolet radiation. In addition to OH masers, SiO and H_2O masers are used to probe the velocities of the inner dust-free zones and accelerating wind zones, respectively (Richards et al. 2014). All three types of masers are critical to understanding the kinematics of dust-driven winds.

Circumstellar 1612-MHz OH masers exhibit double-peaked profiles. The double-peak is a result of the expansion of the OH shell and the radial amplification of 1612-MHz photons from this shell (Engels & Bunzel 2015). From OH masers we can determine the velocity of outflowing material as half the separation of the main twin emission peaks. The peaks represent the blueshifted and redshifted final wind speeds of outflowing material moving towards and away from us, respectively. This expansion velocity can be used to test the dust-driven wind theory:

$$v_{\exp} \propto r_{gd}^{-1/2} L^{1/4}, \qquad (1)$$

where L is the luminosity and r_{gd} is the gas-to-dust ratio; the dust-to-gas ratio has shown strong empirical evidence to scale approximately with the metal content (Habing, Tignon & Tielens 1994; van Loon 2000, 2012; Elitzur & Ivezić 2001). Often OH masers are the only available tool to derive expansion velocities in extragalactic systems as they radiate with an intensity much greater than the alternative, thermal CO line emission.

We can test and refine dust-driven wind theory by observing OH masers in the Large Magellanic Cloud (LMC), which has a metallicity of a half solar for the ISM and for stars formed in the most recent few Gyr (Choudhury, Subramaniam & Cole 2016), and is within close proximity. The well-known distance to the LMC at 50 kpc (Feast 2013) gives us accurate luminosity measurements and the ability to test the dependence of mass-loss on luminosity. What follows is a refined analysis of OH maser searches in the LMC by Wood et al. (1992) and Marshall et al. (2004), as well as new detections from our new observations with the Parkes and Australia Telescope Compact Array (ATCA) radio telescopes. We include samples of OH/IR stars in the Galactic Centre and bulge to extend our metallicity range to supersolar values, in order to determine the dependence of mass-loss on metallicity.

2 DESCRIPTION OF THE SAMPLE

Circumstellar OH masers have been discovered within our Galaxy, and also within the LMC (Table 1). The Hamburg Database (Engels & Bunzel 2015) has compiled thousands of OH maser detections within our Galaxy, yet few have been discovered in the LMC. Previous OH maser searches in the LMC have been completed by Wood et al. (1992), van Loon et al. (1998a), van Loon et al. (2001b), and Marshall et al. (2004) using *IRAS* data for selection criteria. These searches were biased against objects in molecular cloud regions which require better resolution. LMC searches of other maser types have supplemented these searches, including the SiO maser search by van Loon et al. (1996, 2001b) and the water maser searches by van Loon et al. (1998b, 2001b) and Imai et al. (2013).

Following the successful selection method adopted by Marshall et al. (2004), with the added benefit of existing mid-IR spectra obtained with the *Spitzer Space Telescope* (Buchanan et al. 2006; Kemper et al. 2010; Woods et al. 2011), we selected the brightest oxygen-rich (silicate dust) mid-IR sources (which pump the OH maser) with the reddest optical and near-IR colours known in the LMC. These have luminosities $L \gtrsim 20\,000\,L_\odot$. Despite the superior angular resolution of *Spitzer*, all targets are exclusively *IRAS* or *MSX* sources, suggesting that a few (if any) luminous OH/IR stars were missed. Indeed, none other was found in a recent search for extremely dusty luminous red supergiants in the LMC (Jones et al. 2015) based on the *Herschel Space Observatory* far-IR survey HERITAGE (Meixner et al. 2013).

Additionally, we targeted stars that pulsate with very long periods and large amplitudes, ignoring normal Mira variables which have shorter periods, thinner shells, and weaker OH emission. Typical LMC sources pulsate with periods $P \gtrsim 1000$ d and with K-band ($\sim 2.2\,\mu$m) amplitudes $\Delta K \geq 1.2$ mag, as shown in Table 2. As a consequence of their thick envelope of circumstellar dust, these stars are obscured at short wavelengths and are bright in the mid-IR ($F_{25} \gtrsim 0.5$ Jy).

In order to determine how the dusty wind depends on stellar parameters, we have collected two comparison samples of OH/IR stars in the inner Milky Way. We describe these samples in detail in Section 4.2.2, but it suffices to highlight here some of their relevant similarities and differences. Like the LMC sample, both the Galactic Centre and Galactic bulge samples have relatively uniform and well-known distances, OH maser detections, and IR photometry. The Galactic Centre sources have reliable pulsation periods; for the Galactic bulge sources, we determine them for the first time here. By virtue of their OH detection, these represent the most extreme OH/IR populations in those stellar systems. However, because they are dominated by relatively old, low-mass stars – and more massive stars are just too rare to yield examples of the briefest, most extreme phases of evolution – their luminosities are typically lower than those of the LMC sample, $L \sim 10\,000\,L_\odot$. The same selection bias

Table 1. The LMC target sample, including the detections from Wood et al. (1992), van Loon et al. (1998a), and Marshall et al. (2004); J2000 positions are taken from 2MASS and ATCA observations. Also listed are the previously detected OH masers, and whether we detected OH maser emission here (no entry means that the target has not been attempted).

Object name	Alternative names	2MASS position (J2000)		ATCA position (J2000)		Previous OH	This work OH
		RA	Dec.	RA	Dec.		
IRAS 04407−7000	LI-LMC 4	04 40 28.5	−69 55 14			Yes[a,b]	Yes
IRAS 04498−6842	LI-LMC 60	04 49 41.5	−68 37 52	04 49 40.9	−68 37 50	Yes[a]	Yes
IRAS 04509−6922	LI-LMC 77	04 50 40.5	−69 17 32	04 50 40.3	−69 17 35	No[c]	Yes
IRAS 04516−6902	LI-LMC 92	04 51 29.0	−68 57 50	04 51 29.6	−68 57 47	No[a]	Yes
IRAS 04537−6922	WOH S 60	04 53 30.9	−69 17 50				No
IRAS 04545−7000	LI-LMC 159	04 54 10.1	−69 55 58			Yes[c]	Yes
IRAS 04553−6825	WOH G064	04 55 10.5	−68 20 30			Yes[a,c]	Yes
IRAS 04553−6933	LI-LMC 183	04 55 03.1	−69 29 13				No
IRAS 05003−6712	LI-LMC 297	05 00 19.0	−67 07 58			Yes[a]	Yes
IRAS 05280−6910	NGC 1984-IRS1	05 27 40.1	−69 08 05	05 27 41.3	−69 08 02	Yes[c]	Yes
IRAS 05294−7104	LI-LMC 1153	05 28 48.2	−71 02 29	05 28 48.9	−71 02 32	No[a]	Yes
IRAS 05298−6957	LI-LMC 1164	05 29 24.6	−69 55 14			Yes[c]	
IRAS 05329−6957	LI-LMC 1286, TRM 60	05 32 52.3	−67 06 26			Yes[c]	No
IRAS 05402−6956	LI-LMC 1506	05 39 44.8	−69 55 18			Yes[c]	
IRAS 05558−7000	LI-LMC 1790, TRM 58	05 55 21.0	−70 00 03			Yes[a]	Yes
MSX LMC 807	LI-LMC 1280	05 32 37.2	−67 06 56	05 32 37.3	−67 06 57		Yes
MSX LMC 811		05 32 51.3	−67 06 52	05 32 51.3	−67 06 52	Yes[c]	Yes
MSX LMC 815		05 35 14.1	−67 43 56				No
MSX LMC 1207	LI-LMC 182	04 55 06.5	−69 17 09				No

References: [a]Marshall et al. (2004); [b]van Loon et al. (1998a); [c]Wood et al. (1992).

Table 2. The LMC sample with bolometric magnitudes M_{bol}, pulsation periods P, K-band peak-to-peak pulsation amplitudes ΔK, mean K-band magnitudes, and $J - K$ colours from Whitelock et al. (2003). *Spitzer* 8.0-μm (F_8) and 24-μm (F_{24}) flux densities are from the SAGE project (Meixner et al. 2006, 2013), which use IRAC (Fazio et al 2004) and MIPS (Rieke et al. 2004), respectively, on board the *Spitzer Space Telescope* (Werner et al. 2004). Spectral types are from van Loon et al. (2005), except where noted otherwise. We adopt a distance to the LMC of 50 kpc (Feast 2013).

Object name	M_{bol} (mag)	P (d)	ΔK (mag)	K (mag)	F_8 (Jy)	F_{24} (Jy)	$J - K$	Spectral type
IRAS 04407−7000	−7.11	1264[a]	1.23	8.79	0.51	0.68	2.34	M7.5
IRAS 04498−6842	−7.72	1292	1.30	8.08	0.78	0.69	1.86	M10
IRAS 04509−6922	−7.28	1292	1.45	8.59	0.37	0.86[b]	2.21	M10[c]
IRAS 04516−6902	−7.11	1165[a]	1.41	8.72	0.30	0.55[b]	2.32	M9[c]
IRAS 04537−6922				8.06[d]	0.04	1.30	1.27[d]	M3[e]
IRAS 04545−7000	−6.56	1216	1.57	10.13	0.17	0.38	5.70[f]	
IRAS 04553−6825	−9.19[g]	841	0.34	7.09	5.30	13.53[b]	2.60[b]	M7.5
IRAS 05003−6712	−6.20	942[a]	1.59	9.95	0.14	0.19	2.95	M9
IRAS 05280−6910	−7.75[f]			12.87[h]	1.03	24.18[i]		
IRAS 05294−7104	−6.79	1079	1.20	9.21	0.23	0.25	2.97	M8
IRAS 05298−6957	−6.72[f]	1280[f]	2.00[f]	10.29[f]	0.59	1.05	3.54[f]	
IRAS 05402−6956	−6.77	1393	1.80	10.40	0.62	1.00	4.46[f]	
IRAS 05558−7000	−6.97	1220	1.42	9.25	0.33	0.49	3.27	
MSX LMC 807	−6.08[j]			11.93[k]	0.33	0.45		
MSX LMC 811	−6.71[j]			11.12[d]	0.76	1.25	5.2[l]	
MSX LMC 815	−8.00[j]	590[m]		8.14[k]	0.19	0.20[n]	1.36[k]	M4
MSX LMC 1207				11.50	0.12		2.87	

References: [a]Kim et al. (2014); [b]Trams et al. (1999); [c]van Loon et al. (1998a); [d]Cutri et al. (2003); [e]Humphreys (1978); [f]Wood et al. (1992); [g]van Loon et al. (1999); [h]van Loon et al. (2005); [i]van Loon et al. (2001b); [j]Jones et al. (2012); [k]Buchanan et al. (2006); [l]Sloan et al. (2008); [m]Pierce, Jurcevic & Crabtree (2000); [n]van Aarle et al. (2011).

will also have predominantly selected metal-rich stars, which are not present in the LMC.

We have detected four new 1612-MHz circumstellar OH masers in the LMC (IRAS 04509−6922, IRAS 04516−6902, IRAS 05294−7104, and MSX LMC 807) and obtained wind speeds for six others. We successfully observed 13 targets with three discoveries, one serendipitous discovery, and two non-detections; Galactic maser sources (shown in Appendix B) were used to check the point-

ing. We have used the velocities at the peaks of the maser profile to measure the expansion velocity of our sources with an uncertainty of around 1 km s^{-1}. We have also successfully observed one target in the 1665-MHz maser transition, IRAS 05280−6910. Before conducting this survey, only five of the known LMC maser profiles were reliable. We now have 13 reliable maser profiles, doubling the previous LMC sample and bringing us closer to testing stellar wind driving mechanisms. We will describe each in turn in the following

subsections. No emission was detected from any source at 1667 or 1720 MHz.

3 OBSERVATIONS

3.1 The Parkes radio telescope

Targeted observations were done with the 64-m Parkes radio telescope in New South Wales, Australia. The observations were done in 2003 from August 14 to 22 (Marshall et al. 2004), in 2005 (new) from July 8 to 9, and from August 13 to 22, observing the 1612-MHz OH satellite line. The multibeam receiver used a dual polarization setup with 8-MHz bandwidth and 8192 channels yielding 0.18 km s^{-1} channel^{-1} velocity resolution. The observations used a 12-arcmin beam and an 8-MHz bandwith. Most observations were done in frequency-switching mode except for the 2003 observations of IRAS 04498−6842, IRAS 04509−6922, and IRAS 04553−6922, which were done in position-switching mode; integration times for observations are listed in Table 3.

Data were reduced using the CASA ASAP toolkit (McMullin et al. 2007). The data were inspected manually for quality and for radio frequency interference (RFI). Each scan which was deemed reliable

was averaged by polarization and then a line-free baseline was fitted and subtracted with a low-order polynomial. The scans were then averaged and reduced separately for each epoch. Additionally, the collective data for each target were averaged and reduced. All scans were aligned in velocity, weighted by the noise ($T_{\rm sys}^{-2}$), and fitted with another low-order polynomial, which was then subtracted. Any bad data spikes were determined visually and removed from within the file. All spectra were Hanning smoothed to extenuate any potential maser peaks. This process has yielded spectra for each target from the 2003 and 2005 observing sessions, as well as spectra with the combined data. As these sources are highly variable, multiepoch observations have been critical for confirmation.

3.2 The Australia Telescope Compact Array (ATCA)

The data were taken between 2015 March 6 and 8, on 2015 June 11, and between 2016 February 21 and 26, using the 6C, 6A, and 6B array configurations of the ATCA, respectively. We did targeted integrations observing all four OH transitions (1612, 1665, 1667, and 1720 MHz) using the CFB 1M-0.5k correlator configuration with zoom bands. The observations used a synthesized beam of around 7 arcsec and a velocity range of 465 km s^{-1}. During the first

Table 3. Results of recent maser searches in the LMC.

Object name	$v_{\rm exp}$ (km s^{-1})	Parkes (P) or ATCA (A) epoch	Integration time (h)	Velocity at peaks (km s^{-1}) Blue	Red	$F_{\rm int}$ (mJy km s^{-1}) Blue	Red	σ (mJy)
IRAS 04407−7000	8.35	P 2003	8.6	222.8	239.5, 237	9.6	35.5	5.9
		P 2005	1.7		240, 237		89.8	8.8
		Combined	10.2	223?	240, 237		105.8	4.8
IRAS 04498−6842	13.0	P 2003	13.8	246.3		22.9		8.2
		A 2015	4.6	246.3	272.3	8.2	44.5	10.6
		Combined	18.4	246.3	272.3	67.3	6.4	6.3
IRAS 04509−6922	11.4	P 2003	5.0	254.2	274.7	5.1	3.4	10.1
		P 2005	22.7	255.9	278.6	53.3	44.2	3.9
		A 2015	4.1	256		101.5		26.7
		Combined	31.8	255	278.6	75.2	52.1	3.7
IRAS 04516−6902	10.0	P 2003	8.5		287.3		16.0	7.0
		A 2015	12.6		287.3		30.6	3.8
		Combined	21.1	267.1	287.1	13.3	30.4	3.4
IRAS 04537−6922	?	A 2016	10.8					3.7
IRAS 04545−7000	7.7	P 1992	1	258.7	274			6.1
		P 2005	4.5	258.7	274	191.5	37.6	6.1
		Combined	4.5	258.7	274	191.5	37.6	6.1
IRAS 04553−6825	23.8	P 2003	0.8	253.4, 263	281, 300.9	1709, 414	11.7, 8.2	12.7
		P 2005	0.6	253.4, 263	281, 300.9	1346, 289	74.1, 52.6	14.0
		Combined	1.4	253.4, 263	281, 300.9	1417, 272.6	32.3, 21.9	9.8
IRAS 04553−6933	?	A 2016	10.8					3.6
IRAS 05003−6712	?	P 2003	7.2	287?	269.5	87.1		6.7
		P 2005	3.4		269.5	40.5		5.8
		Combined	10.6	243	269.5	65.8		4.2
IRAS 05280−6910	20.6	P 1992	1	255	289	419	398	17
		A 2016	5.7	258.1	292.6	131.1	147.3	11.5
IRAS 05294−7104	10.3	A 2016	9.8	269.7	290.3	9.6	34.2	5.5
IRAS 05298−6957	10.5	P 1992	1	271	292	519	448	17
IRAS 05402−6956	10.5	P 1992	1	263	284	334	181	17
IRAS 05558−7000	8	P 2003	7.7	265	281.5	18.5	11.7	5.7
		P 2005	3.4	265	281.5	68.7	52.5	5.9
		Combined	11.2	265	281.5	70.1	51.0	4.1
MSX LMC 807	8.15	A 2015	9.3	306.4	322.7	19.8	12.1	4.6
MSX LMC 811	8.25	A 2015	9.5	302.4	318.9	151	188	4.3
MSX LMC 815	?	A 2015	14.1					4.5
MSX LMC 1207	?	A 2016	10.8					3.8

two observations, we aimed the telescope directly at our primary targets (MSX LMC 807 and MSX LMC 815). The third observation used a position-switching technique to get full *uv* coverage of our third primary target, IRAS 04516−6902, while getting partial coverage on two secondary targets, IRAS 04509−6922 and IRAS 04498−6842. Our two secondary sources could not fit within the primary beam of a single pointing; thus, the need arises to alternate fields to observe with coverage similar to that of the shape of a Venn diagram with pointings separated by ∼13 arcmin. The fourth observation was split, observing the faint detection of IRAS 04516−6902, and the non-detection MSX LMC 815. The fifth, sixth, and seventh observations were aimed directly at our primary targets (IRAS 04553−6933, IRAS 05294−7104, and IRAS 05280−6910).

The ATCA data were inspected, flagged, and calibrated, using the MIRIAD package (Sault, Teuben & Wright 1995). The visibility data were then transformed into three-dimensional data cubes. The source-finding package DUCHAMP (Whiting 2012) was used to search for maser sources within the 28 arcmin full width at half-maximum of each of the fields. For the resulting peaks, our intended targets, and any other potential targets from Riebel et al. (2012, 2015) or SIMBAD, a spectrum was extracted for a region covering the size of the synthesized beam (∼7 arcsec). All spectra for each epoch were combined and weighted by $1/\sigma^2$, where σ is the standard deviation determined from the line-free channels of the displayed spectrum.

3.3 Parkes and ATCA combined H I Maps

In addition to the Parkes and ATCA observations, we have also included 1420-MHz H I data from the Staveley-Smith et al. (2003) combined ATCA and Parkes multibeam H I maps. Peaks in the H I spectra indicate the likely systemic velocities of our sources. While some of our sources lie outside these H I regions, they provide supporting evidence for sources which lie in higher density regions of the LMC. For each source in our LMC sample, a spectrum was extracted using a 1-arcmin region centred on the sources. The resulting spectra have been plotted below the maser spectra in Section 4 to indicate the likely systemic velocity.

4 RESULTS

4.1 Individual maser sources

4.1.1 IRAS 04407−7000

The OH maser emission from the dusty AGB star IRAS 04407−7000 was initially detected with the ATCA (van Loon et al. 1998a). The initial detection showed a single peak at 240 km s^{-1}; we now present subsequent observations with Parkes (Fig. 1). We see a degree of variability between the 2003 and 2005 observations. With the first observation, we see two peaks at around 237 and 240 km s^{-1}. With a peak separation of 3 km s^{-1}, it is unlikely a measure of the full expansion velocity, rather substructure within the circumstellar envelope. We also see a much smaller peak at 223 km s^{-1} in the 2003 observation. For the much shorter 2005 observation, we see the peaks at 237 and 240 km s^{-1}, flanked by two smaller tentative peaks at 214 and 261 km s^{-1} but an overall increase in noise. When the spectra are combined and weighted by the noise, the dominant profile is that of the 2003 observation. Using a cross-spectrum fitting technique (see Appendix C), we have fitted a UVES spectrum of IRAS 04407−7000 from the ESO reduced spectra data archive to that of IRAS 04498−6842 using molecular
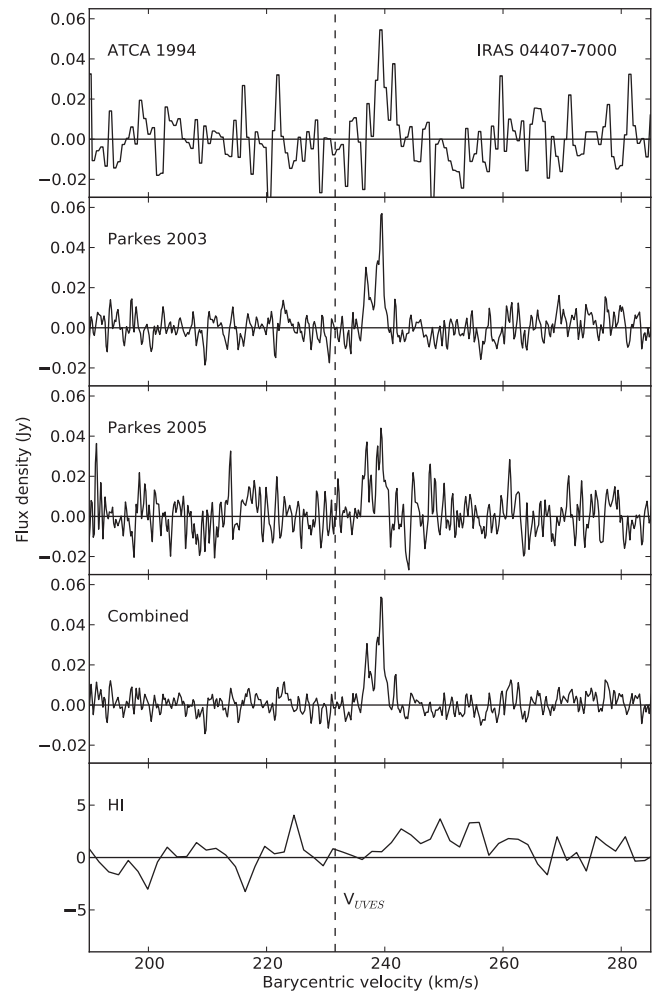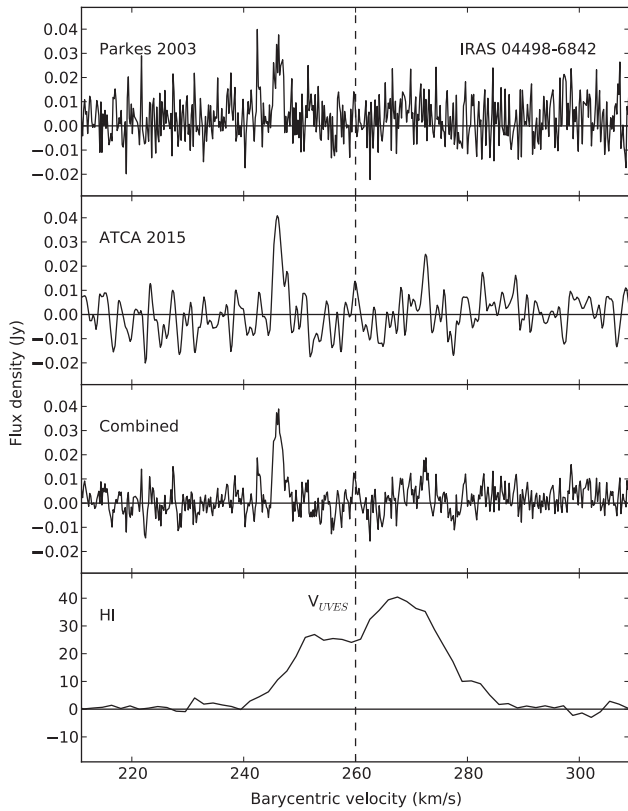

Figure 1. OH 1612-MHz maser emission from IRAS 04407−7000 with the velocity derived from cross-spectrum fitting of UVES spectra denoted by $V_{\rm UVES}$.

bandheads around 8440 Å. We have used a systemic velocity of 260 km s^{-1} for IRAS 04498−6842, assumed from its maser profile. From the phase shift, we calculate a systemic velocity for IRAS 04407−7000 of 231.6 km s^{-1} (denoted by $V_{\rm UVES}$), confirming the smaller blue maser peak at 223 km s^{-1} and the maser profiles of both sources.

4.1.2 IRAS 04498−6842

IRAS 04498−6842 was observed in 2003 with a clear peak at 246 km s^{-1} (Fig. 2). The new observation with the ATCA has confirmed the peak at 246 km s^{-1} and revealed a red counterpart at 272 km s^{-1}. The Parkes multibeam H I data of our target peak around 260 km s^{-1}. As we expect the H I to come from the LMC disc, and our source is likely to have a similar stellar velocity, this provides evidence for our detection. Additionally, we have used the systemic velocity derived from this source's maser profile as a reference to fit both IRAS 04407−7000 and IRAS 04516−6902, and the velocities of all three maser profiles are consistent with our results. IRAS 04498−6842 is one of the more extreme stars within our sample (possibly an RSG, or super-AGB star), with an M10 spectral type (van Loon et al. 2005) and high luminosity. Thus,

Figure 2. OH 1612-MHz maser emission from IRAS 04498−6842 with the velocity used as a model for the cross-spectrum fitting of UVES spectra denoted by $V_{\rm UVES}$.

it is not surprising that our maser profile yields a high expansion velocity of 13 km s^{-1}.
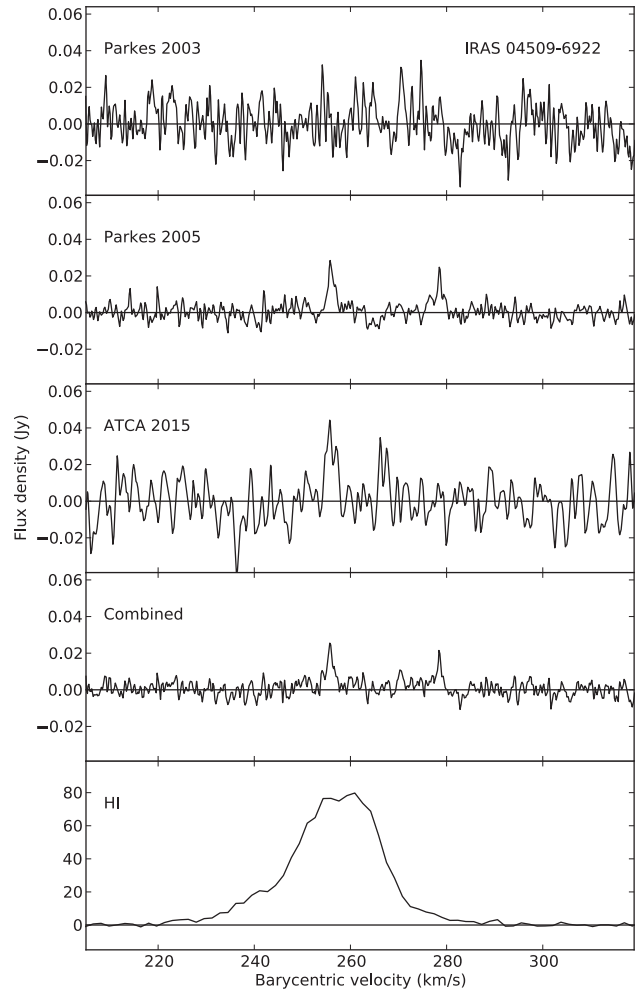
4.1.3 IRAS 04509−6922

IRAS 04509−6922 is a new detection, with a clear double-peaked profile centred around 268 km s^{-1} (Fig. 3). The profile expansion velocity of 11.5 km s^{-1} is also high within our sample but expected, given its low temperature and high luminosity. We see a peak around 255 km s^{-1} over all three observations, but the red component is clear only in the much longer integration in the 2005 observation. The peak in H I at around 260 km s^{-1} supports our detection.

4.1.4 IRAS 04516−6902

IRAS 04516−6902 was observed in 2003, with no clear maser emission. Given our new ATCA data (Fig. 4), it seems that the small peak at around 285 km s^{-1} in our Parkes observation is in fact a maser component. We also see a much fainter peak in the combined data around 267 km s^{-1}, yielding an expansion velocity of 10 km s^{-1}. Using the same cross-spectrum fitting technique as was adopted for IRAS 04407−7000, we calculate a systemic velocity of 278.8 km s^{-1}. This velocity lies directly between our two maser peaks, confirming our maser profile.

4.1.5 IRAS 04545−7000

The maser profile of IRAS 04545−7000 does not seem to vary drastically over our two epochs (Fig. 5). The detection has a clear
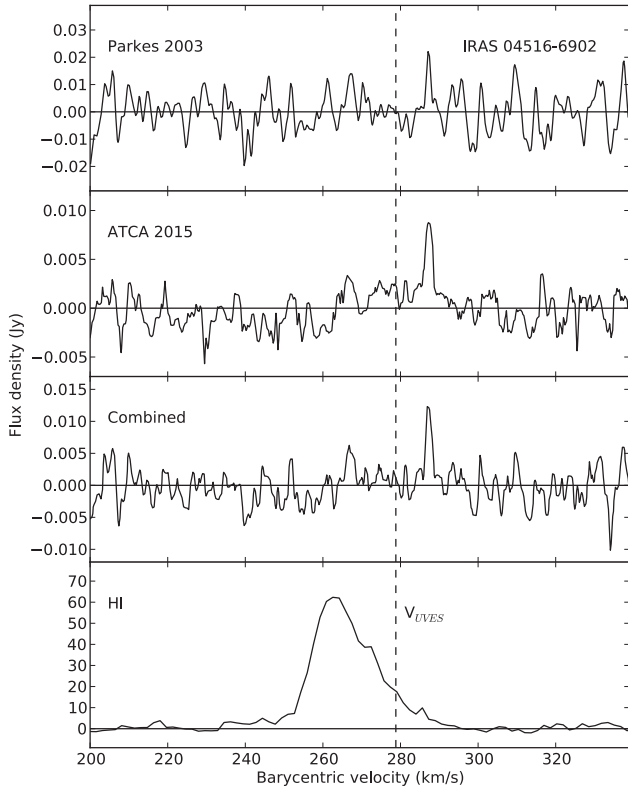

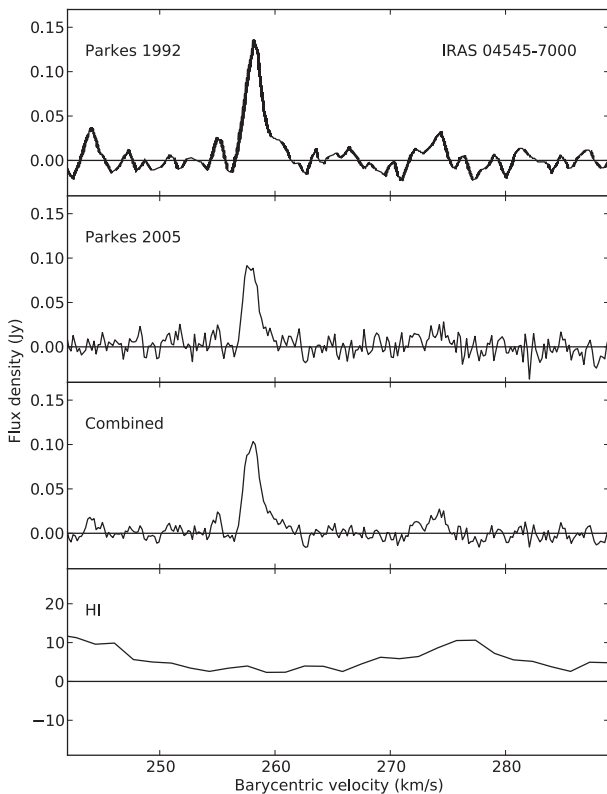**Figure 3.** OH 1612-MHz maser emission from IRAS 04509−6922.

blue-asymmetry, a phenomenon described in Marshall et al. (2004), which has been suggested as a consequence of the contribution of amplified stellar light. While IRAS 04545−7000 is not a very luminous source, it is one of the most highly reddened sources in our sample with a $(J − K)$ colour of 5.7 mag.

4.1.6 Red supergiant IRAS 04553−6825

IRAS 04553−6825 has shown the most prominent OH maser emission in the LMC with a peak over 600 mJy around 253 km s^{-1} (Fig. 6). This RSG is one of the largest known stars, with an estimated radius of 1540 R$_\odot$ (Levesque et al. 2009). This object has been studied in depth, and has been observed in OH (Wood, Bessel & Whiteoak 1986; Marshall et al. 2004), H$_2$O (van Loon et al. 1998b), and SiO (van Loon et al. 1996). In addition to its peak at 253 km s^{-1}, there are three additional peaks at 262, 281, and 300 km s^{-1}. Given the systematic velocity of 278 km s^{-1} taken from the SiO maser detection, we can say with some certainty that the maser profile extends from its prominent blue peak at 253 km s^{-1} to its smallest peak at 300 km s^{-1}. The existence of the two interior peaks has been suggested by Marshall et al. (2004) to be indicative of a second expanding dust shell, flowing primarily in a direction across the sky.

Figure 4. OH 1612-MHz maser emission from IRAS 04516−6902 with the velocity derived from cross-spectrum fitting of UVES spectra denoted by V_{UVES}.

Figure 5. OH 1612-MHz maser emission from IRAS 04545−7000.
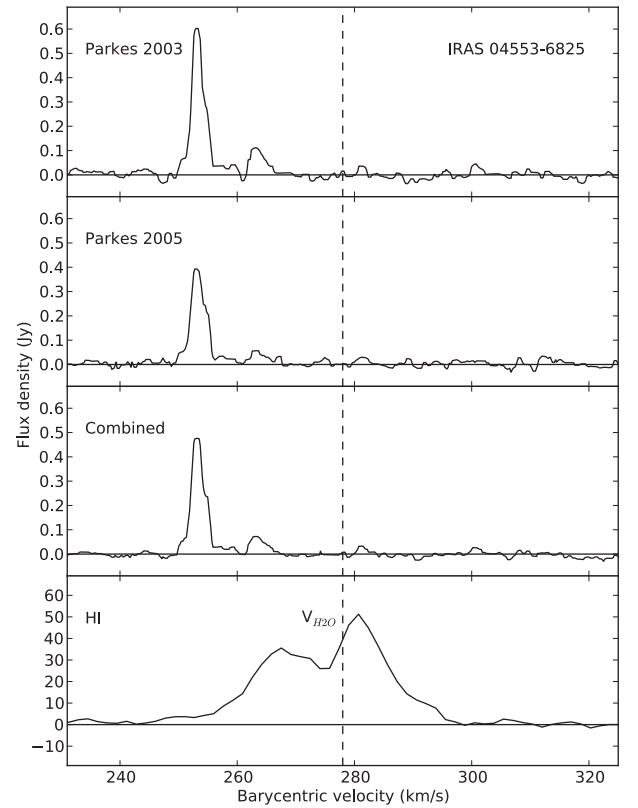
Figure 6. OH 1612-MHz maser emission from IRAS 04553−6825 with the H_2O maser velocity from van Loon et al. (2001b) denoted by V_{H2O}.

4.1.7 IRAS 05003−6712

IRAS 05003−6712 is the least luminous source of our sample (Fig. 7). We see a clear peak at 269 km s^{-1} in both epochs, but the second peak is unclear. The source fits all other criteria expected of an OH/IR star, but the secondary peak may be below the detection limit of past observations. From our SED modelling (explained in Section 4.2), we expect an expansion velocity around 10 km s^{-1} (assuming a metallicity of half that of the Sun). The skewed shape of the peak at 269 km s^{-1} suggests that we need to be looking for the missing redshifted peak. Nevertheless, the maser profile remains unclear.

4.1.8 Red supergiant IRAS 05280−6910

The maser emission of the RSG IRAS 05280−6910 was originally observed at 1612 and 1665 MHz with Parkes in 1992 (Wood et al. 1992). We have since observed the source using the ATCA and re-vealed five maser peaks at 1612 MHz and some interesting structure at 1665 MHz (Fig. 8). The IR source was originally misidentified as the cluster NGC 1984. High-resolution near- and mid-IR imaging has successfully identified the stellar counterpart (van Loon et al. 2005). IRAS 05280−6910 is highly obscured and extremely bright in the mid-IR but shows little variability. This source has also shown 22-GHz H_2O maser emission (van Loon et al. 2001b). The lack of symmetry within these maser spectra as well as variability of not only the flux but also of the location of maser components remains puzzling. We would also expect the mainline 1665-MHz detection to probe the inner shell of OH and thus lie within the 1612-MHz maser profile. We will discuss this source further in Section 5.
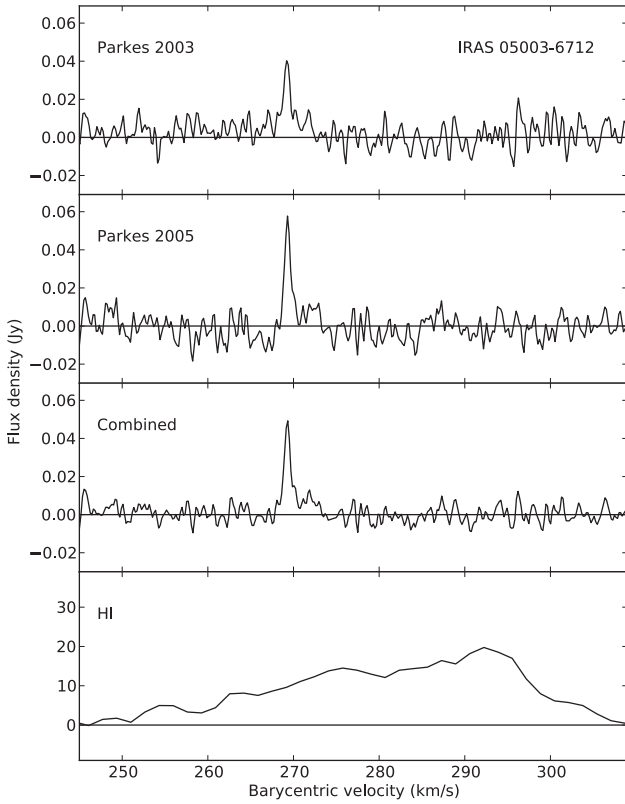
Figure 7. OH 1612-MHz maser emission from IRAS 05003−6712.

4.1.9 IRAS 05294−7104

IRAS 05294−7104 was not initially detected during the 2003 observation but was detected with our more recent longer ATCA observation (Fig. 9). It is highly reddened with a $(J − K)$ colour of 2.97 mag, with a long pulsation period lasting 1079 d and an expansion velocity of 10.3 km s^{-1}. It seems that the initial observation lacked the signal-to-noise ratio required for detection.

4.1.10 IRAS 05298−6957

IRAS 05298−6957 resides in a cluster and thus has a cluster metallicity of 0.4 solar metallicity. This source pulsates with a ΔK of 2 mag, and has an initial mass of $4\,M_\odot$ yr^{-1} (van Loon et al. 2001a). The source has a clear double-peaked profile yielding an expansion velocity of 10.5 km s^{-1} (Wood et al. 1992). IRAS 05298−6957 has shown silicate in absorption, yet lies in a region of the LMC sample colour–magnitude diagram which is dominated by carbon-rich chemistry (Sargent, Srinivasan & Meixner 2011). This is a well-known but often ignored issue, which is seen in a number of OH/IR sources (cf. Zijlstra et al. 1996; van Loon et al 1997; Trams et al. 1999).

4.1.11 IRAS 05402−6956

OH maser emission from IRAS 05402−6956 was detected with Parkes in 1992 (Wood et al. 1992) and is known to be within 3 arcmin of an H II region. The expansion velocity from the original observation was 10.5 km s^{-1}, but, as the emission was detected with a low signal-to-noise ratio, it is unclear whether the profile includes the outermost peaks.
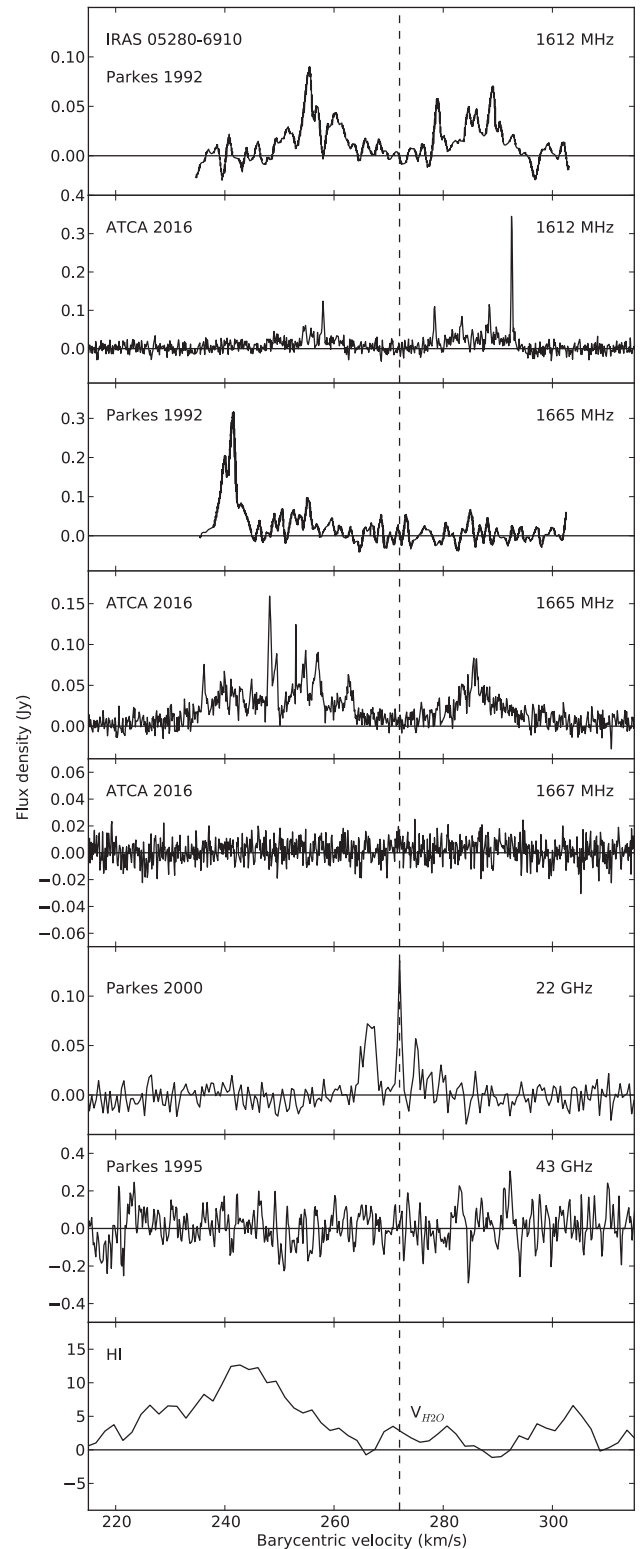

Figure 8. OH 1612- and 1665-MHz maser emission from IRAS 05280−6910 with the SiO and H$_2$O maser velocity from van Loon et al. (2001b); the water maser velocity has been plotted and denoted by V_{H2O}.
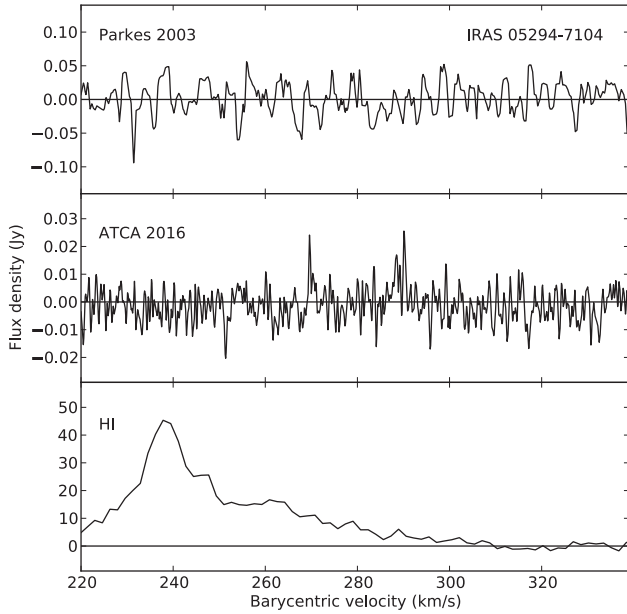
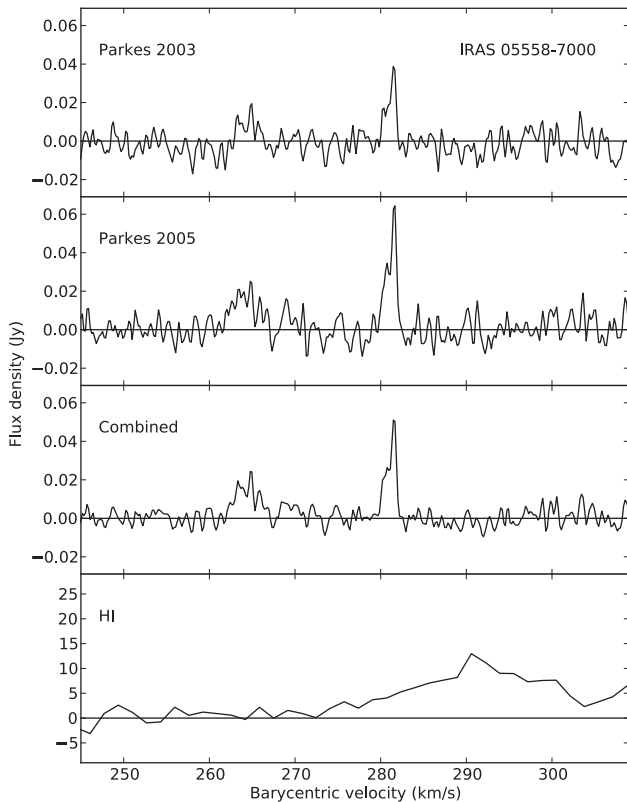**Figure 9.** OH 1612-MHz maser emission from IRAS 05294−7104.

Figure 10. OH 1612-MHz maser emission from IRAS 05558−7000.

4.1.12 IRAS 05558−7000

IRAS 05558−7000 lies at the edge of the LMC. The source has two clear peaks at 265 and 281 km s^{-1}, in both epochs of observation, yielding an expansion velocity of 8 km s^{-1} (Fig. 10).
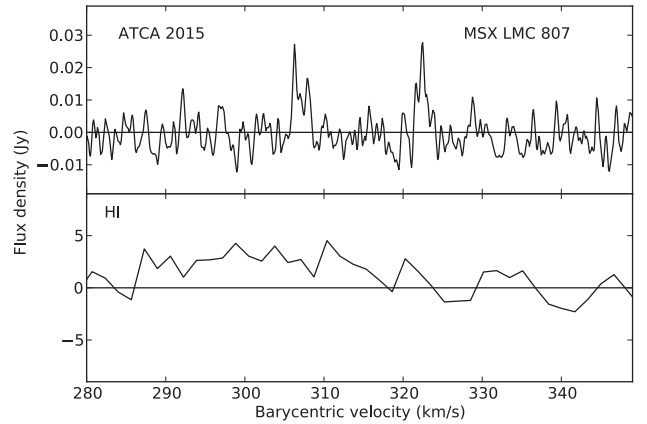

Figure 11. OH 1612-MHz maser emission from MSX LMC 807.

4.1.13 MSX LMC 807

MSX LMC 807 is a dusty O-AGB star with a $(J - K)$ colour of 3.7 mag and $M_{\rm bol} = -6.6$ (Whitelock et al. 2003). This star has shown 10 μm silicate emission (Buchanan et al. 2006) but a low IR luminosity comparable to many C-AGB stars in the LMC (Buchanan et al. 2006). This is one of our new OH maser detections from ATCA observations. We see a clear double-peaked profile yielding an expansion velocity of 8 km s^{-1} (Fig. 11).

### 4.1.14 MSX LMC 811 (IRAS 05329−6708)

MSX LMC 811 has been found to be the true counterpart of the maser emission thought to originate from IRAS 05329−6708. While IRAS 05329−6708, MSX LMC 807, and MSX LMC 811 were previously resolved in the IR, the original Parkes observation of IRAS 05329−6708 did not have the resolution to resolve IRAS 05329−6708 into MSX LMC 807 and MSX LMC 811. Thus, the observation yielded partial emission from both MSX LMC 807 and MSX LMC 811 (Fig. 12). This can be seen in the four peaks found in the 1992 observation, which show the two similar wind speeds with different systemic velocities. As the *MSX* survey resolved our IR sources, we have now done the same with the OH maser emission. The star is extremely red with a $(J - K)$ colour of 5.2 mag; the expansion velocity of 8.5 km s^{-1} is also reasonable for the source.

4.1.15 MSX LMC 815

MSX LMC 815 is an M4 O-AGB star with a *K*-band magnitude of 8.14 and has shown a number of spurious spikes at 1612 MHz but no clear maser profile (Fig. 13). H_2O maser emission has been detected at 237 km s^{-1} by Imai et al. (2013); yet, the H_2O maser detection was a very weak detection, weaker than many H_2O maser detections of RSGs in the Galaxy. This source has a short pulsation period of 590 d typical of our galactic sources. We expect that the 1612-MHz maser flux should peak at close to 25 per cent of the 35-μm flux due to the efficiency of the pumping mechanism (Elitzur, Goldreich & Scoville 1976; Marshall et al. 2004). As this source has an $F_{24} = 0.22$ Jy, the maser emission would likely be below our detection limit.
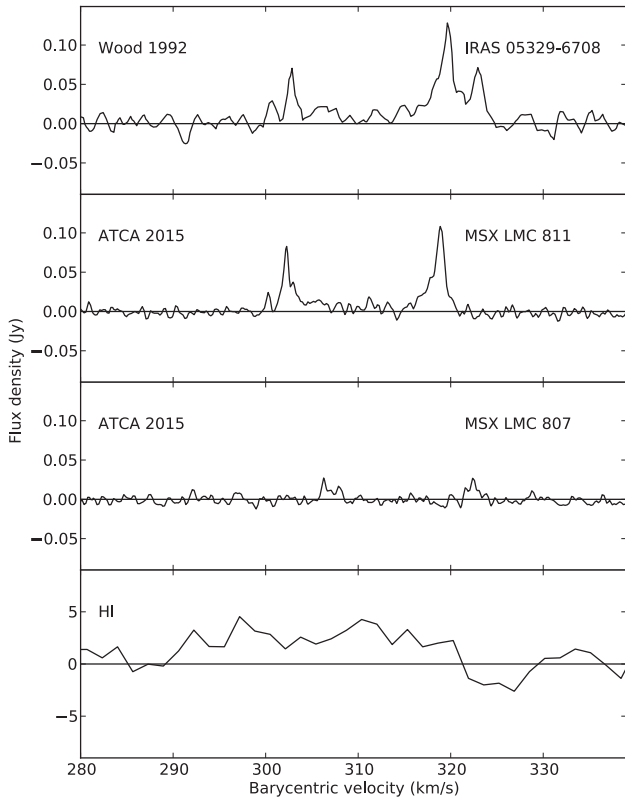
Figure 12. OH 1612-MHz maser emission from MSX LMC 811 and the newly discovered MSX LMC 807. Originally thought to originate from IRAS 05329−6708, the true components of the maser emission have now been identified.
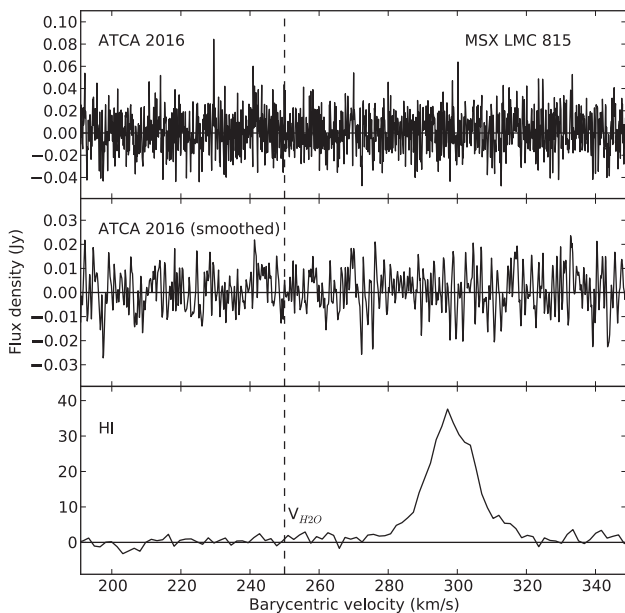
Figure 13. OH 1612-MHz non-detection from MSX LMC 815, with the velocity of the water maser detection made by Imai et al. (2013) denoted by V_{H2O}.

4.2 Modelling the SED

4.2.1 LMC sources

We have modelled all our AGB and RSG sources in the LMC with radiatively driven wind models produced with the DUSTY code (Elitzur & Ivezić 2001). Two important outputs from the DUSTY 1D radiation transfer code are the SED of the source modelled and the expansion velocity of the dust-driven wind. The SEDs for the LMC sources are shown in Fig. 14, and the results are listed in Table 5 (shown later). The models use a blackbody for the central star and assume dusty envelopes of warm silicates from Ossenkopf, Henning & Mathis (1992), with varying effective temperatures and inner boundary dust temperatures and the standard MRN (Mathis, Rumpl & Nordsieck 1977) grain size distribution.

As these are variable sources, to accurately reproduce the true SED with our models, we can only fit one epoch of photometry. We have thus used the *Spitzer* IRAC and MIPS photometry (Fazio et al. 2004; Rieke et al. 2004), plotted in red, and fitted them with DUSTY models using a χ^2 fitting technique. The available 2MASS *JHK* photometry are not of the same epoch and are more sensitive to the effects of geometry. We have thus ignored them in our source fitting. The fitting technique calculates the best fit of the photometry to 5900 models of varying optical depth, central blackbody temperature, inner dust temperature, and normalization factor. We obtain luminosities for the best-fitting models (plotted with dashed lines) assuming a distance of 50 kpc to the LMC. We expect these luminosities to be more accurate than for Galactic sources because of the well-determined distance to the LMC. These results constrain the derived parameters of the source at the time that the *Spitzer* photometry data were taken (2005 July–November). The current stellar parameters would have fluctuated since as a result of the sources' variability.

For each of our sources, we have compiled all available photometry from 2MASS (Cutri et al. 2003), DENIS (Cioni et al. 2000), *AKARI* (Yamamura et al. 2010), *MSX* (Egan, Price & Kraemer 2003), and *IRAS* (Beichman et al. 1988), and overplotted them in the SED fitted with small open circles; we expect our SED to lie between the stellar variations. We have additionally overplotted *Spitzer* IRS spectra (Lebouteiller et al. 2011), shown in solid black. It should be noted that the best DUSTY model was fitted to photometry, independently of the IRS spectra. In most cases, the model successfully reproduces the shape of the photometry and spectra well, which lends credence to the fit solution. Our choice of dust optical constants will affect the final result. The dust mineralogy will change as the central star evolves (Dijkstra et al. 2005; Verhoelst et al. 2009), and our inability to compensate for this effect will introduce a degree of uncertainty.

We ran the DUSTY code in its radiatively driven wind mode, whereby it solves the hydrodynamical equations for the radial dependence of the density and for the velocities of the gas and dust separately (their difference is the 'drift' speed). It is the velocity of the gas – which dominates the mass by far – which we can measure from the OH maser profiles, but the velocity of the dust can be greater by a factor of a few if the wind density is relatively low. If, however, the drift speed is underestimated, then the SED fitting would yield a dust mass-loss rate which is too low and (assuming the gas-to-dust ratio is correct) also a total mass-loss rate which is too low. Ramstedt et al. (2008) found a discrepancy between the mass-loss rates derived using DUSTY and those derived from modelling the CO line emission, with the former always yielding lower values. However, if the drift speed was underestimated, then the
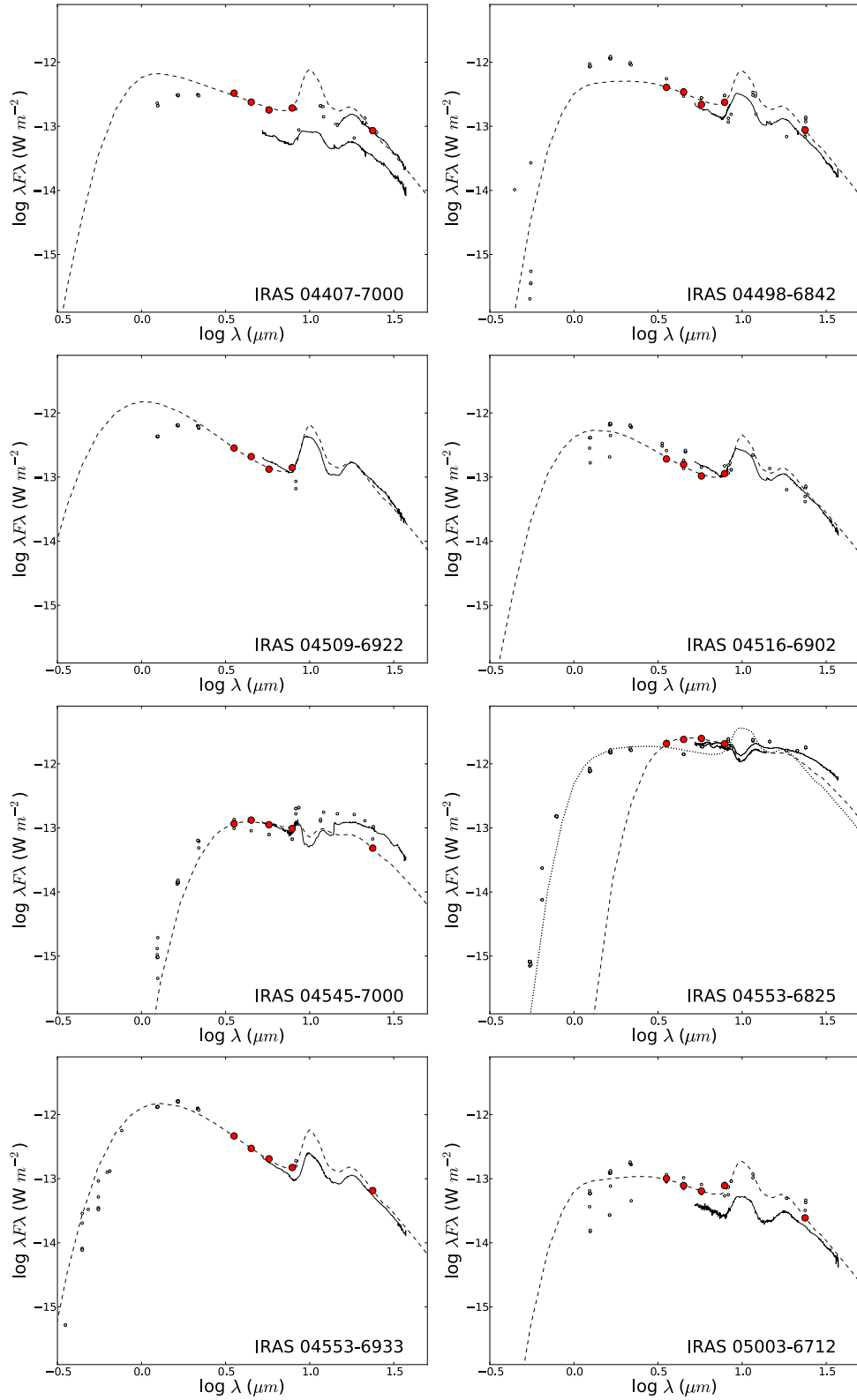
Figure 14. The SED fitting of DUSTY models to our LMC sources, with our best-fitting model (dashed line), *Spitzer* IRS spectra (in solid black), *Spitzer* IRAC and MIPS photometry (in red), and the remaining available photometry (small open circles).
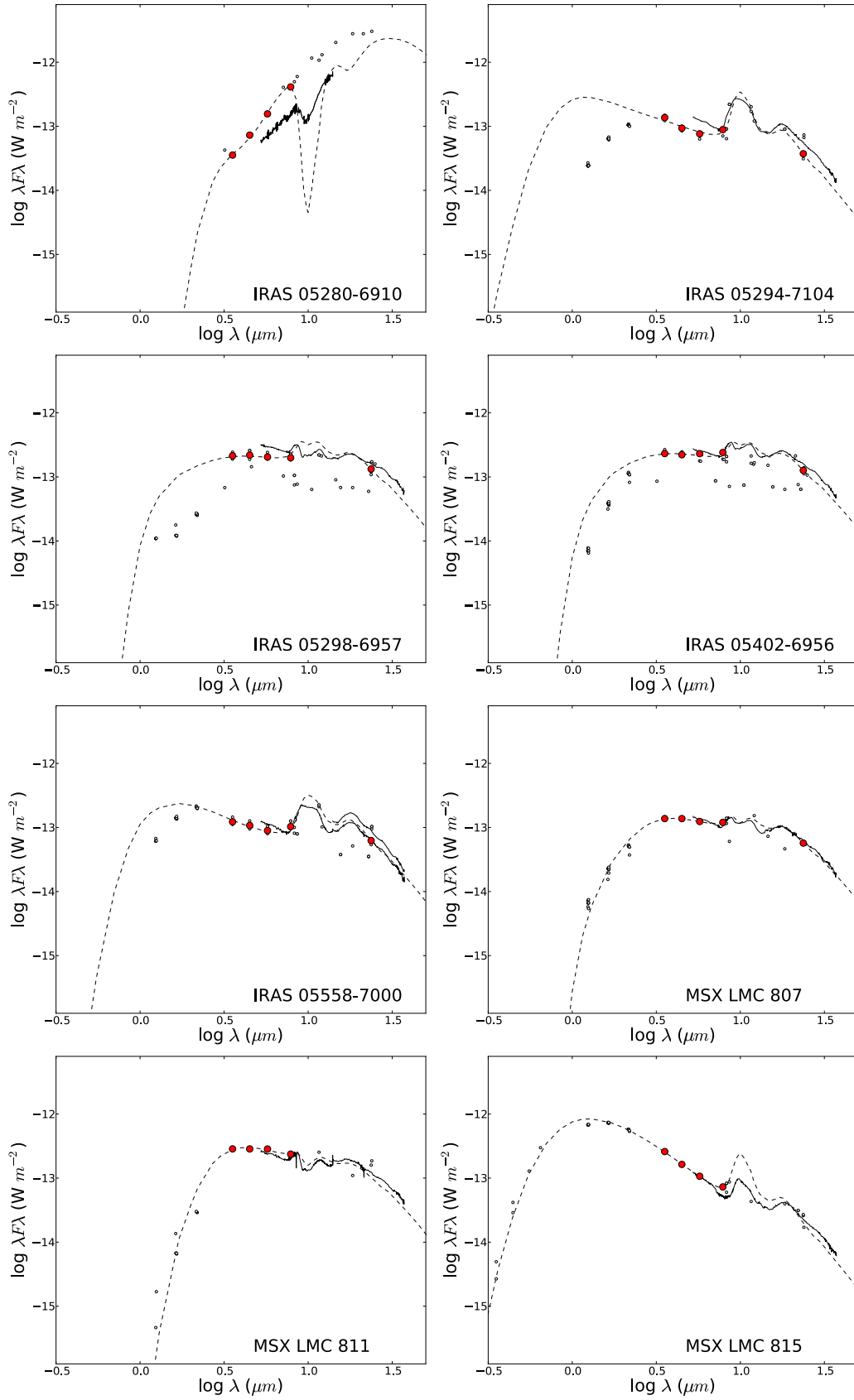
Figure 14 – *continued*

heating of the CO molecules would also have been underestimated and thus CO mass-loss rates would be derived that are too high.

The power of the description of the wind incorporated in DUSTY lies in the fact that the results can be scaled for different dust contents and luminosities according to equation (1) and $\dot{M} \propto r_{gd}^{1/2} L^{3/4}$ (Elitzur & Ivezić 2001) without changing the optical depth – it is the latter which determines the shape of the SED. This is, however, a simplification as the shape of the SED (and acceleration of the wind) depends on the distance from the star where the dust forms. This inner radius is set by imposing a fixed dust formation temperature. While it scales with luminosity as $L^{1/2}$, it has a subtle dependency on the temperature of the star as the grain opacity is wavelength dependent (it therefore also depends on the grains' optical properties). Also, the acceleration of the wind will be somewhat different depending on the apparent size of the star, whereas it is assumed that all stellar flux arises from one point. These effects mostly affect the emission from the warmest dust at near- to mid-IR wavelengths. An outer limit to the size of the envelope is assumed to be 10^4 times the inner radius, which is typical, given the stars we study are near the end of an extended period of heavy mass-loss. The emission from the coldest dust at far-IR wavelengths depends on this choice but not in a sensitive way.

We have fitted the photometry with models of effective temperatures ranging from 2700 to 3700 K in steps of 100 K, and inner dust temperatures ranging from 600 to 1400 K in steps of 200 K, each with 100 models spanning a logarithmic range of optical depths from 0.1 to 50. A comprehensive analysis of the interdependency of these inputs has been presented by Ramstedt et al. (2008). Given all the above caveats and assumptions (and departures from spherical symmetry, see below), it becomes clear that a precise error analysis is impractical. The formal errors on the fitting of trends we observe between different parameters therefore include both measurement uncertainties and fitting inaccuracies, as well as variations in the parameters which we assumed to be fixed.

Within our sample we see varying degrees of silicate in absorption and emission and strong attenuation from dust at shorter wavelengths. We see two sources (IRAS 04553−6825 and IRAS 05280−6910) where the models struggle to fit the general SED. This is likely due to a non-spherical symmetry of the dust envelope in these sources. These unique sources will be further discussed in Section 5. There are two further sources (IRAS 04553−6933 and MSX LMC 815) where the model struggles to fit both the optical and mid-IR data. Both of these sources show no OH maser emission, and extremely high modelled expansion velocities. These sources may not be optically thick enough for the IR radiation to pump the maser or these may be binary systems.

4.2.2 Galactic Centre and Galactic bulge samples

In addition to our LMC sample, we have also modelled sources from the Lindqvist et al. (1992) Galactic Centre sample of OH/IR stars, and the Jiménez-Esteban & Engels (2015) Galactic bulge sample of more extreme highly reddened OH/IR stars, to serve as comparison samples at higher metallicity; we have used pulsation periods from Wood et al. (1998) and those we derive (Appendix D) for the Galactic Centre and bulge respectively. Assuming a distance of 8 kpc to these regions, and using a similar modelling method, DUSTY models, and sources of photometry, we have successfully modelled 70 Galactic Centre and 21 Galactic bulge OH/IR stars. The distribution of the resulting luminosities is shown along with the values from the LMC in Fig. 15 (shown later). We can see
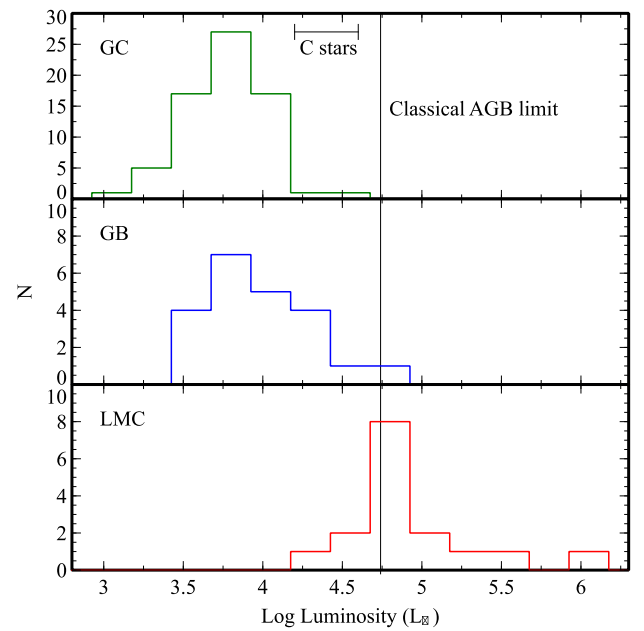
Figure 15. Galactic bulge, Galactic Centre, and LMC luminosity distributions.

the void in our histogram where at luminosities between those of our lower luminosity Galactic sources and higher luminosity LMC sources sources are dominated by carbon-rich chemistry (C stars).

As the photometry is more sensitive to extinction, we have fitted the SED using all available photometry, expecting the best-fitting model to fit the median SED. Distances are also less certain for our Galactic sources and we expect this to contribute to the uncertainty in these luminosities. To correct for interstellar extinction, we have used the Schultheis et al. (2014) extinction maps from 8 to 8.5 kpc and applied an extinction curve. Using the closest value (typically within several arcminutes) for the $(H − K)$ colour excess, we have applied the extinction law from Rieke & Lebofsky (1985), using interpolated values to fit the wavelength bands associated with our photometry. This was done for all Galactic bulge and Galactic Centre sources except for IRAS 17030−3053, which was not covered by the extinction maps. As a result, we assign it a value of $A_K = 0.15$ mag, adopted from Jiménez-Esteban & Engels (2015). There has been increasing evidence that the reddening law varies within the Galactic Centre (Nataf et al. 2016; Xue et al. 2016); yet, our results are not dramatically affected by this result. This reddening variation is caused by populations of small dust grains and mainly affects shorter wavelength photometry. The results of the DUSTY modelling of the SEDs for the Galactic Centre sources are shown in Appendix A1, whereas the modelling results for those in the Galactic bulge are shown in Appendix A2.

As the Galactic Centre and some of the Galactic bulge sources lie in crowded fields, we expect a small percentage of photometry points towards shorter wavelengths to come from other sources. We see that our Galactic Centre sources show a variety of silicate in both emission and absorption. This is a stark contrast to the Galactic bulge sources, which all show silicate strongly in absorption, an expectation of this more extreme sample by design. These bulge sources may also be members of the Galactic disc, in the foreground of the bulge. Catchpole et al. (2016) have shown that a number of sources assumed to be members of the bulge have had a wide range of distances. This may introduce a large source of uncertainty in our derived luminosities.

5 DISCUSSION

5.1 LMC target population

Our observing programme targets sources with known but unclear OH maser profiles, as well as sources which are deemed good candidates. In general, we target highly luminous and reddened AGB and RSG sources with long pulsation periods and large pulsation amplitudes. Within our current sample, IRAS 04407−7000 and IRAS 05003−6712 only exhibit one maser peak. As these sources and their maser emission are highly variable (Harvey et al. 1974), subsequent observations are much more likely to give us a double-horned maser profile and expansion velocity.

We expect the LMC to harbour several thousand OH masing sources (Dickey et al. 2013). Our much smaller observed sample likely indicates a sensitivity limit. OH masers are predicted to be excited by line overlapping of far-IR OH lines (e.g. Elitzur, Goldreich & Scoville 1976; Bujarrabal et al. 1980). To excite OH masers, these far-IR OH lines are required to be optically thick. Therefore, only the most luminous, high-mass-loss-rate AGB stars and RSGs can produce OH masers detectable with our current instruments; the ability to sustain these masers will also depend on metallicity (OH abundance and dust emission). The LMC AGB stars are also dominated by carbon-rich chemistry, decreasing the population of OH masing sources. OH/IR stars of low enough mass not to become carbon stars will also be less luminous, thus restricting the expected detectable sample to the much rarer massive AGB stars ($\gtrsim 4\,\mathrm{M_\odot}$). In order to further understand the mass-loss mechanism and the effects of varying metallicity and luminosity, we will need to continue to discover more sources in the LMC, and extract what we can from our current sample. The fact that we detected additional sources serendipitously means that more OH masers must be awaiting detection at the current sensitivity limits.

5.1.1 IRAS 04553−6825 (WOH G64)

IRAS 04553−6825 is known to be highly non-spherical (Roche, Aitken & Smith 1993; Ohnaka et al. 2008), originally suggested on the basis of its optical brightness and strong silicate feature. This was later suggested by van Loon et al. (1999) on the basis of its maser characteristics. The maser source has been observed in OH, showing four OH maser peaks. The non-spherical nature of this source makes it quite hard to model. While we were able to successfully model and fit the 10 μm silicate feature in absorption, something we see in the *Spitzer* and *ISO* spectra (cf. Trams et al. 1999; van Loon et al. 1999), we are not able to simultaneously fit the general SED. We have therefore overplotted a secondary model (plotted with a dotted line) where we do fit the general SED (Fig. 14). The two models differ slightly in both luminosity and mass-loss, with a luminosity between 340 000 and 454 000 L$_\odot$ and a mass-loss rate between 3.1×10^{-4} to 5.8×10^{-4} M$_\odot$ yr^{-1}. We expect that our models represent the range of possible luminosities and mass-loss rates of this unique source. Ohnaka et al. (2008) suggested that the source is likely to a have a dusty torus which we are observing pole-on. This explanation is consistent with our results.

5.1.2 Mass-loss of IRAS 05280−6910

The maser emission from IRAS 05280−6910 is unique. First, the source shows maser emission at 1612 and 1665 MHz but not at 1667 MHz. Secondly, the maser profiles are very irregular with a number of peaks which have changed in amplitude and velocity since 1992. And, thirdly, the 1665-MHz maser profiles, which should probe a region closer to the star (Richards & Yates 1998), extend (at the blue end) to velocities outside of the 1612-MHz profiles. All of these peculiarities come to heel as we look more closely at the polarization data (Fig. 16). We see that this source is strongly circularly polarized at 1665 and 1612 MHz, alluding to magnetic activity close to the star. We suspect Zeeman splitting at two locations in the 1665-MHz spectrum centred at 248.9 and 285.8 km s^{-1}. The separation of these bright maser peaks suggests an upper limit of the magnetic fields of around 1.2 and 2.2 mG, respectively. The peaks at 257 and 262.7 km s^{-1} are unlikely to be a Zeeman pair as the resulting magnetic field would be around 10 mG and would result in an $\sim$1 km s^{-1} split in the 1612-MHz spectra at this velocity, which we do not see. We have used Stokes $I + V/2$ for RHCP and $I - V/2$ for LHCP (IAU convention), where RHCP is the rotation of the electric field vector in a counterclockwise direction as the wave travels from the source to the observer along the line of sight.

The magnetic activity coupled with the large velocity range of the maser profile may be suggestive of bipolar outflows, collimated by the magnetic fields. The bluest 1665-MHz maser peaks may either be more highly accelerated, localized 'bullets' as opposed to the more uniform wind farther out which is probed by the 1612-MHz masers, or they may be associated with interstellar masers as they peak at the H I velocity. The complete absence of 1667-MHz emission must be due to quenching as a result of the strong 1665-MHz masers. Sources like VY CMa and IRAS 04553−6825 have shown similar complex profiles with many maser peaks and asymmetric envelopes (Cohen et al. 1987); yet, IRAS 05280−6910 also has a distinctly unique SED. Studies of VY CMa have shown a number of arcs and knots, which may also be present in our source (Humphreys et al. 2005; Humphreys, Helton & Jones 2007).

The DUSTY modelling of IRAS 05280−6910 yields an expected expansion velocity of 13.6 km s^{-1}. This is considerably lower than the observed value of 20.6 km s^{-1}. We expect this disparity to come from something more than uncertainty or unrealistic modelling. What we may be observing is a near edge-on dusty torus, similar to IRAS 04553−6825, which is highly obscured along our line of sight. This result would also support the idea that the source has bipolar outflows. These outflows could explain the models' slow calculated expansion velocity (which could be expected along our line of sight), while not necessarily leading to such a low gas-to-dust ratio or high mass-loss rate.

We see an obvious difference between our DUSTY models and the IRS spectrum of IRAS 05280−6910. The *Spitzer* IRS spectrum of this source shows silicate in absorption, but not to the same degree as our modelled SED. The observed absorption feature may be partially masked by the nearby RSG WOH G347 (van Loon et al. 2005), a source which shows silicate in emission. A further investigation of this object in the optical and at high angular resolution in the mid-IR would certainly be worthwhile.

5.2 Stellar winds at different metallicities

We now examine the stellar wind expansion velocities of the sources in our LMC, Galactic Centre, and Galactic bulge samples. In OH/IR stars, the mass-loss process and the outflow acceleration are driven by radiation pressure on dust grains. In these dense environments, the gas is dynamically coupled with dust through friction, and the outflow behaves like one single fluid. As these stars produce mainly silicate dust, and the production of silicates is limited by initial
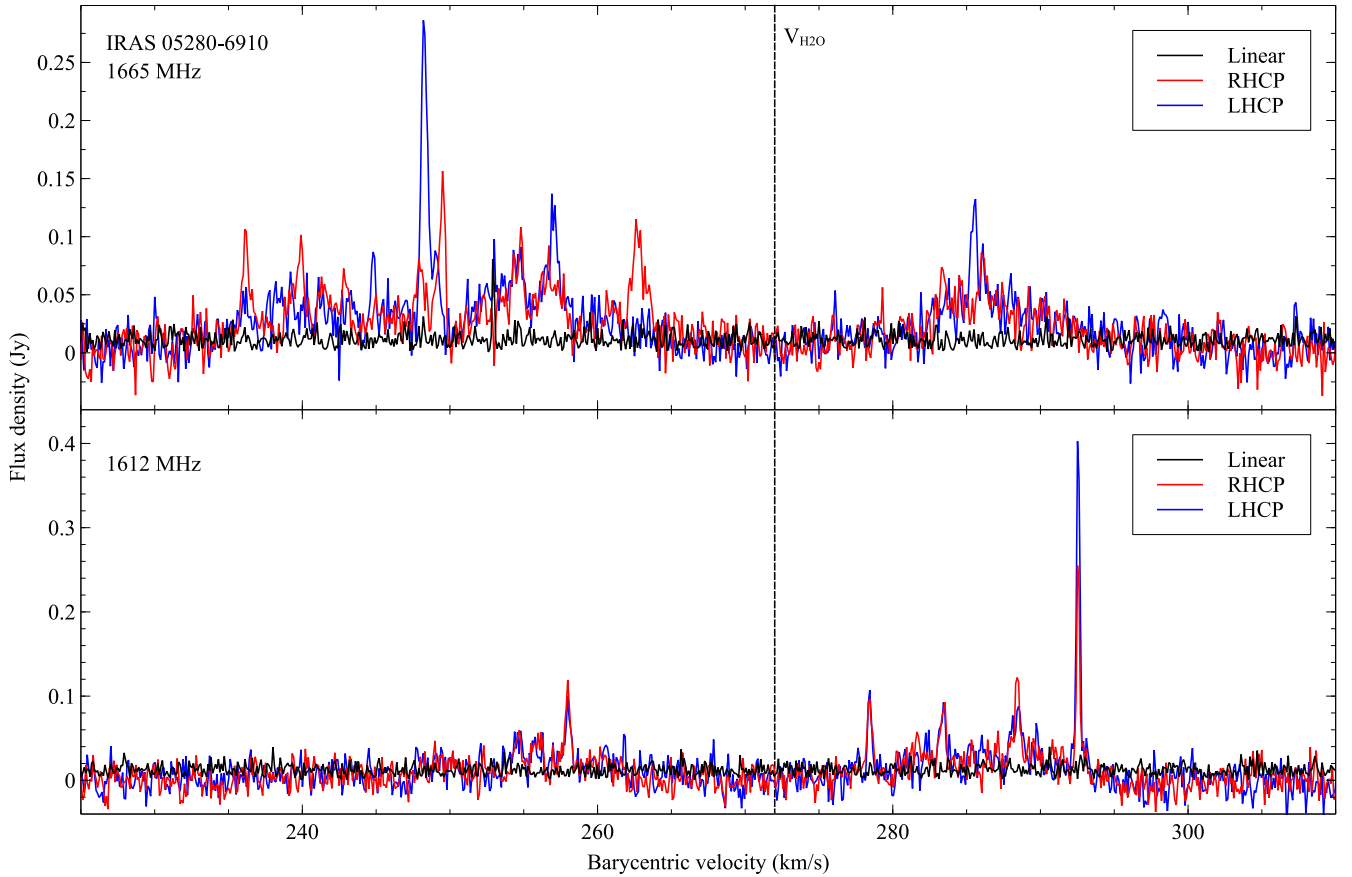
Figure 16. The left- and right-hand circular polarization of the (top) 1665-MHz and (bottom) 1612-MHz maser detections of IRAS 05280−6910; the systemic velocity from the water maser emission from van Loon et al. (2001a) is indicated with V_{H2O}.

metallicity,[1] lower metallicity yields a slower wind. We expect that at lower luminosity there is less radiation pressure to force the dust grains outwards and drive the wind, and therefore a slower expansion velocity; in general, this is observed in both the LMC and Galactic samples, as it was shown by Marshall et al. (2004), as well as the following work (Fig. 17).

The LMC and Galactic samples have several differences, including very different luminosities and pulsation periods. The LMC sample is biased towards the most luminous sources as they are distant and obscured, and only the most massive and luminous AGB stars remain oxygen-rich in the heavy mass-loss phase. The lower luminosity sources are thus dominated by carbon-rich stars. As a result, we expect a selection bias within the LMC. The LMC sample is also biased towards longer pulsation periods as the OH maser emission is brightest in the most evolved and highest mass-loss sources. The Galactic bulge sample is a collection of the most extreme OH/IR sources in the Galactic bulge and generally lack pulsation periods. We have used data from the Vista Variables in the Via Lactea (VVV) survey (Minniti et al. 2010) to derive periods for seven of our Galactic bulge sources (Appendix D). The Galactic Centre sources tend to be lower mass and less extreme but still within the superwind phase of mass-loss. The fact that this is an older population may be contributing to the sample's lack of higher

mass sources, similar to those within our LMC sample. In addition to differences within the sample, we have differences in the quality of our radio observations (Table 4). While we have significantly less angular resolution for our Galactic bulge sample, we use only resolved and reliable maser profiles; all observations have spectral resolutions around 1 km s^{-1}.

The majority of stars in the Galactic Centre have metallicities at or above solar, with a small population of low-metallicity sources (Wood, Habing & McGregor 1998; Do et al. 2015). The Galactic bulge has a metallicity typically peaking at a near solar value, with a sharp cut-off just above solar, and a tail towards lower metallicity (Zoccali et al. 2003). We expect that our extreme sources likely lie towards the higher end of this metallicity range.

We see that at a similar luminosity, the Galactic bulge sources have lower expansion velocities than those of the Galactic Centre sources (Fig. 17). We see this same effect even more so in the LMC sample with a metallicity (Z) even lower, at half solar. This is consistent with what we expect from simple dust-driven wind theory (e.g. van Loon 2000). We have fitted the expansion velocities from our LMC sample with respect to their luminosities. Our fit ($v_{\rm exp} = 0.118L^{0.4}$) is then scaled to a solar metallicity (a factor of 2) typical of the Galactic samples, which fits well within these samples. We have used these results to derive a new relation for expansion velocity:

$$v_{\rm exp} \propto ZL^{0.4}. \qquad (2)$$

We have dramatically increased the number of measured wind speeds from previous studies which relied on five accurate wind

---

[1] Contrary to C-stars in which the dredge-up events can enhance the amount of carbon initially available in the atmosphere.
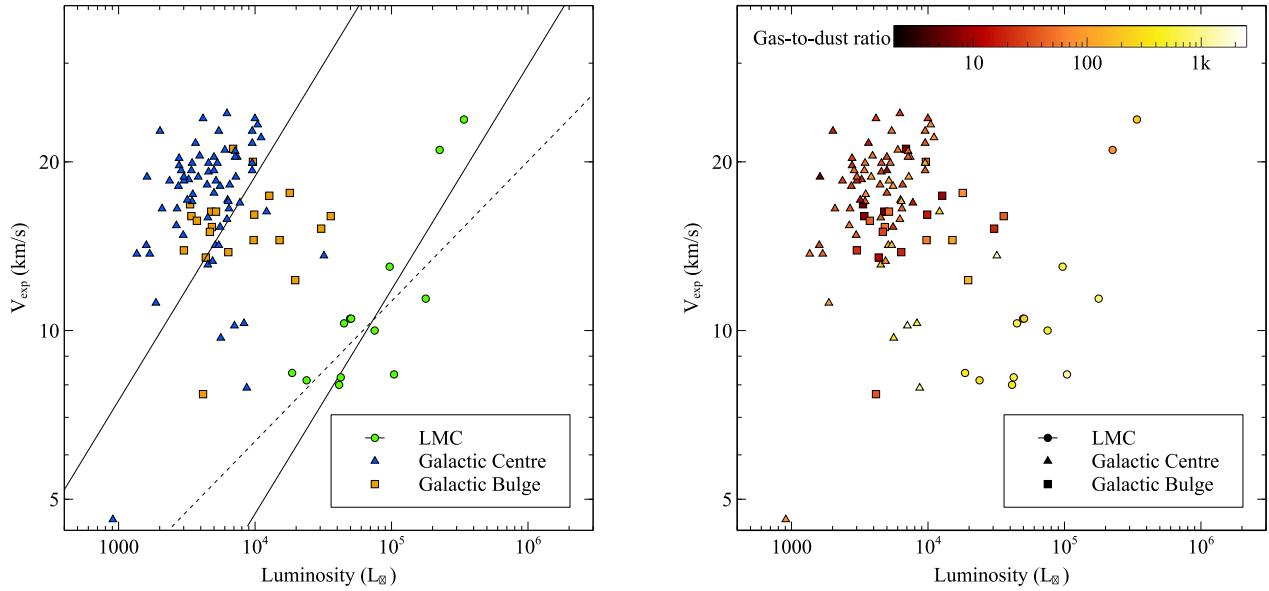
Figure 17. Left-hand panel: the observed wind speed as a function of luminosity for our sample of OH/IR stars in the LMC and Galactic samples. The LMC sample is fitted with a power law ($v_{exp} = 0.118L^{0.4}$). The power law (solid black) is then scaled to a metallicity characteristic of the Galactic sample (a factor of 2). We have derived a new relation: $v_{exp} \propto ZL^{0.4}$, which fits well with our samples. We compare our relation to that of dust-driven wind theory: $v_{exp} \propto r_{gd}^{-1/2}L^{0.25}$ (dotted line). Right-hand panel: the observed wind speed as a function of luminosity with the gas-to-dust ratio represented in colour, as derived from the scaling of SED models.

Table 4. The resolution of the radio observations of our LMC and Galactic samples.

Sample	Telescope	Spectral resolution (km s^{-1})	Angular resolution
Galactic Centre	VLA	1.36[a]	6–8 arcsec
Galactic bulge	Parkes	0.9[b]	12 arcmin
	Effelsberg	1.1[b]	8 arcmin
LMC	Parkes	0.18	12 arcmin
	ATCA	0.4	7–8 arcsec

*References*: [a]Lindqvist et al. (1992); [b]te Lintel Hekkert et al. (1991).

speeds. Using our larger sample, we find that our updated relation: $v_{exp} = 0.118L^{0.4}$ more accurately fits the data (Fig. 17). Nevertheless, these results make several assumptions. We assume spherical symmetry within our sources, scattering of photons to affect the sources' collective radiation pressure, and uniformity of dust properties throughout our samples. We also assume a homogeneous metallicity within each of our samples, which we know not to be the case.

We can see the individual effects of different parameters on the expansion velocity more clearly in Figs 18 and 19. In Fig. 18, we compare the expansion velocity against the gas-to-dust ratios we derive through SED fitting (described further in the following section). We see that the expansion velocity is dependent on the gas-to-dust ratio. These samples have been fitted with a power law which is expected to follow $v_{exp} \propto r_{gd}^{-0.5}$. The actual fit: $v_{exp} \propto r_{gd}^{-0.15}$ is much shallower due to the effects of luminosity on the wind speeds. The higher luminosities of the LMC result in higher LMC wind speeds and a shallower fit. When we compare the expansion velocities to mass-loss rate and pulsation period (Fig. 19), we see no clear correlation. The scatter is mostly due to differences in
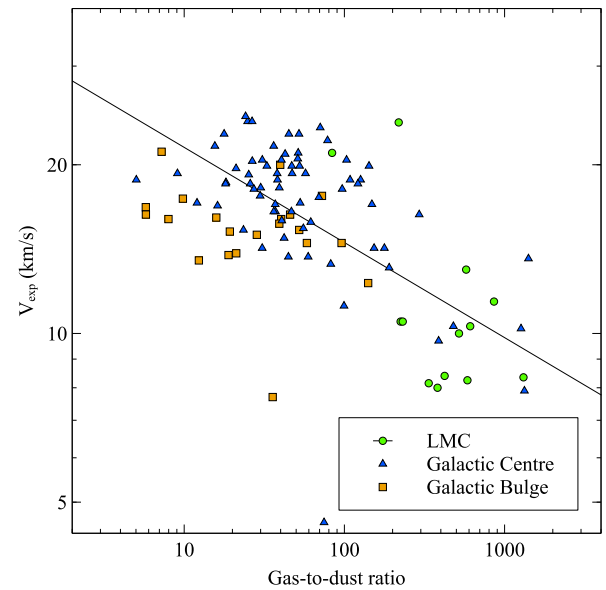
Figure 18. The observed wind speed as a function of gas-to-dust ratios which we have derived from SED fitting. The samples have been fitted with a power law which is expected to fit: $v_{exp} \propto r_{gd}^{-0.5}$ (equation 1). The actual fit: $v_{exp} \propto r_{gd}^{-0.15}$ is much shallower due to the effects of luminosity on the wind speeds. The higher luminosities of the LMC result in higher LMC wind speeds and a shallower fit.

luminosity and metallicity between and within the samples. This is contrary to the expectations of the DARWIN models (Höfner et al. 2016), which do predict a correlation of expansion velocity and mass-loss rate. Likely, the correlation reflects the evolution along the AGB, whereas our samples are naturally biased towards the endpoints of evolution.
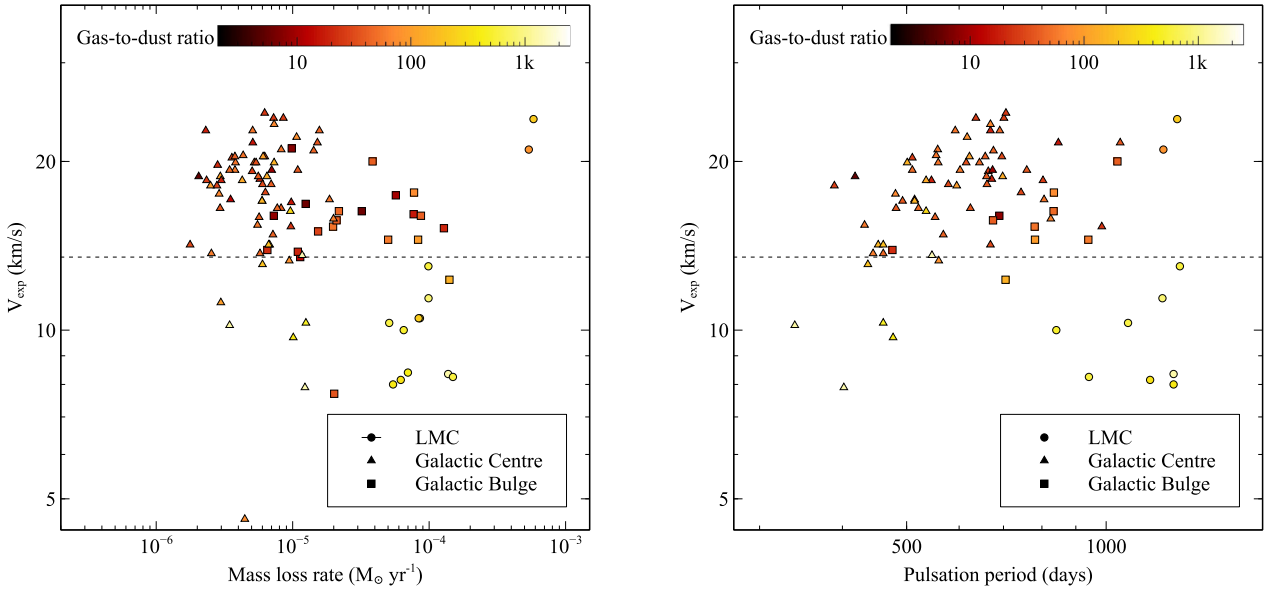
Figure 19. The observed wind speed as a function of mass-loss rate (left-hand panel) and pulsation period (right-hand panel), with the gas-to-dust ratio represented in colour. Mass-loss rates and gas-to-dust ratios are derived from the scaling of SED models (discussed further in Section 5.3). The dotted lines indicate the change from the higher to lower metallicity sample, which, as we have shown, will affect the expansion velocities. Looking at the Galactic samples, there does not seem to be any clear correlation between expansion velocity and either mass-loss rate or pulsation period.

Table 5. The LMC inferred gas-to-dust ratios (r_{gd}) and mass-loss rates ($\dot{M}$) from scaling the resulting DUSTY expansion velocities ($v_{exp,DUSTY}$) to the expansion velocities obtained from circumstellar OH maser profiles ($v_{exp,OH}$). Luminosities (L) and optical depths specified at 10 μm (τ) are derived from the SED fitting of DUSTY models which assume the effective temperature ($T_{eff,DUSTY}$) and inner dust temperature (T_{inner}). Mass-loss rates scale in proportion to $L^{3/4}(r_{gd}\rho_s)^{1/2}$, where the dust grain bulk density (ρ_s) is 3 g cm^{-3}; measured effective temperatures (T_{eff}) are from van Loon et al. (2005), unless stated otherwise.

Object name	L (10^3 L$_\odot$)	T_{eff} (K)	$v_{exp,OH}$ (km s^{-1})	$v_{exp,DUSTY}$ (km s^{-1})	$T_{eff,DUSTY}$ (K)	T_{inner} (K)	τ	$\dot{M}$ (M$_\odot$ yr^{-1})	r_{gd}
IRAS 04407−7000	104	3008	8.35	21.4	3400	800	0.4	1.4×10^{-4}	1312
IRAS 04498−6842	97	2500	13.0	22.1	3400	1000	0.7	9.8×10^{-5}	576
IRAS 04509−6922	178	2500	11.4	23.6	3700	600	0.1	9.9×10^{-5}	859
IRAS 04516−6902	75	2667^b	10.0	16.1	2900	600	0.3	6.5×10^{-5}	519
IRAS 04545−7000	19		7.7	11.2	3200	1200	4.9	7.0×10^{-5}	422
IRAS 04553−6825	340–454	3008	23.8	24.9	3300	1400	8.62	5.8×10^{-4}	218
IRAS 04553−6933	176			21.9	2900	600	0.1	$^a5.9 \times 10^{-5}$	
IRAS 05003−6712	23	2667		14.5	3700	1000	0.8	$^a3.3 \times 10^{-5}$	
IRAS 05280−6910	225		20.6	13.6	3400	350	13.4	5.4×10^{-4}	84^d
IRAS 05294−7104	45	2890	10.3	17.5	3600	800	0.4	5.1×10^{-5}	610
IRAS 05298−6957	50	4000^b	10.5	11.1	3000	800	2.0	8.6×10^{-5}	224
IRAS 05402−6956	51		10.5	11.3	2700	800	2.2	8.4×10^{-5}	231
IRAS 05558−7000	42	3400^b	8.0	11.0	2700	600	0.7	5.4×10^{-5}	381
MSX LMC 807	24		8.2	10.6	2900	1000	3.2	6.2×10^{-5}	336
MSX LMC 811	42		8.3	14.1	2700	1200	5.6	1.5×10^{-4}	586
MSX LMC 815	97	3100^a		24.9	3000	800	0.1	$^a2.5 \times 10^{-5}$	
Sample median values:									
Galactic Centre	5		18.5	8.5	3000	1200	2.8	6.0×10^{-6}	45
Galactic bulge	6		15.7	4.7	3200	800	19.5	2.2×10^{-5}	28
LMC	63		10.3	15.3	3100	800	0.8	7.7×10^{-5}	422

Notes. ^{a}Calculated using the assumed gas-to-dust ratio of 400; ^{b}Buchanan et al. (2006); ^{c}García-Hernández et al. (2009); ^{d}Unlikely true gas-to-dust ratio; further explained in Section 5.2.

5.3 Gas-to-dust ratios in the LMC

Using our SED modelling, we are able to estimate the expected expansion velocity of our sources. These estimates, calculated using the DUSTY code, rely on the assumption that the winds are dust driven and spherically symmetric. We have also measured expansion velocities from OH maser emission, and can scale our gas-to-dust

ratio, assumed to be 200, by the square of the ratio between the expected and measured expansion velocities (equation 1). Using this method, we have derived gas-to-dust ratios for all of our LMC sources shown in Table 5.

Adding up all of the refractory elements within oxygen-rich dust and scaling to the metallicity of the LMC, we expect a gas-to-dust ratio ∼ 500. The interstellar gas-to-dust ratio (r_{gd}) of the LMC has

also been shown by Roman-Duval et al. (2014) to be between 380 and 540. Our median r_{gd} of 422 agrees well with previous estimates but lies towards the lower end of these estimates. This may be due to our bias towards the most metal rich sources. Our higher r_{gd} (lowest metallicity) objects, IRAS 04407−7000 and IRAS 04509−6922, have far lower inferred metallicities than the rest of the sample. All of these sources have quite reliable OH maser detections, with well-fitted SEDs. These stars are within close proximity to each other, lying within the same south-east region of the LMC, towards the Magellanic Bridge. We can speculate that it may be due to either a lower efficiency of dust formation in these stars or they may have formed from lower metallicity gas, possibly originating from the Small Magellanic Cloud (SMC; see Olsen et al. 2011). These are not likely to be members of the small subset of counterrotating sources found by Olsen et al. (2011); as extreme oxygen-rich sources are rare in the SMC, the counterrotating subset is a small fraction of the whole LMC population and the kinematics of the three sources are consistent with the rest of our LMC sample.

We derive median gas-to-dust ratios of 45 and 28 for the Galactic Centre and Galactic bulge, respectively. We see a little difference between the results of our Galactic bulge fitting technique and the fitting by Jiménez-Esteban & Engels (2015). We derive similar luminosities and mass-loss rates, yet find few cases where our best-fitting models have similar optical depths. It was suggested by Jiménez-Esteban & Engels (2015) that the existence of these oxygen-rich Galactic bulge sources can be explained if they have metallicities at or above solar metallicity, which is consistent with our derived gas-to-dust ratios. Our Galactic sources may be alpha-enhanced, which would increase the abundance of elements like Si, Ti, and Mg, and thus increase dust production. Our bias towards the highest metallicity sources may be magnified by this additional alpha-enhancement.

There is quite a large range of gas-to-dust ratios in our three samples. When we compare them with respect to luminosity and expansion velocity (Fig. 17), we see a clear difference between our Galactic and LMC samples. When we compare our luminosities and mass-loss rates (Fig. 20), we see a clear trend irrespective of gas-to-dust ratio. We also see that the Galactic bulge sources tend to have higher mass-loss rates than the other two samples, expected from this more extreme sample.

The idea that there may be two different OH/IR populations within our Galaxy was originally suggested by Wood et al. (1998), where sources with expansion velocities lower than 18 km s^{-1} were expected to have a metal content 2.1 times lower than sources with higher expansion velocities; our results suggest that this is not the case. We find a slightly higher median gas-to-dust ratio for our sources with velocities less than 18 km s^{-1}.

5.4 Mass-loss as a function of gas-to-dust ratio, luminosity, and pulsation period

By employing our new gas-to-dust ratios and using equation (1), we have derived an empirical mass-loss prescription which includes the luminosity (L), pulsation period (P), and gas-to-dust ratio (r_{gd}): $\dot{M} = 4.2 \times 10^{-11} L^{0.9} P^{0.75} r_{gd}^{-0.03}$ (where luminosity is in L$_\odot$ and the pulsation period is in days); normalizing this prescription to a typical source, we arrive at the following relation:

$$\frac{\dot{M}}{M_\odot \, yr^{-1}} = 1.06^{+3.5}_{-0.8} \times 10^{-5} \left(\frac{L}{10^4 \, L_\odot}\right)^{0.9\pm0.1}$$

$$\times \left(\frac{P}{500\,d}\right)^{0.75\pm0.3} \left(\frac{r_{gd}}{200}\right)^{-0.03\pm0.07}. \qquad (3)$$

The function for the mass-loss has been fitted using a non-linear least-squares-fitting technique, to all sources within the three samples and with complete data. The prescription suggests mass-loss rates of 1.18×10^{-5} M$_\odot$ yr^{-1} for a typical source with a luminosity of 10 000 L$_\odot$, pulsation period of 500 d, and gas-to-dust ratio of 200. This is typical for Mira variables and Galactic sources but not our LMC sources with higher luminosities, longer pulsation periods, and higher gas-to-dust ratios. Fig. 20 shows a comparison of the parameter dependence of the mass-loss rates computed with DUSTY with the parameter dependence of the mass-loss rates from our new formula. There is a general correlation of mass-loss with pulsation period, and a much tighter correlation with luminosity. We do not see a strong dependence of gas-to-dust ratio on the mass-loss rate. This suggests that the mass-loss is insensitive to metallicity.

We have also computed mass-loss prescriptions which include only two of the three mass-loss parameters. These prescriptions have been compared to our three-parameter prescription on the basis of their ability to correctly predict the mass-loss rate given by DUSTY; the comparison of these prescriptions is shown in Fig. 21. There is little difference between our three-parameter prescription and our prescription with only luminosity and pulsation period, reflecting the insensitivity of mass-loss to gas-to-dust ratio and, presumably, to metallicity.

It is possible that no single prescription can accommodate the diversity of all OH/IR stars. We have also fitted our individual samples with all three of our mass-loss parameters but would urge caution in using these fits. The limited ranges of the parameters within each of the three samples make these fits much less reliable; the uncertainties on the derived parameters reflect this to some extent, but the fits are overall not nearly as convincing as for the combined sample. The dependence on luminosity (the most reliably fit parameter) is very similar between the three samples, although there is a hint of a trend for a weaker luminosity dependence at higher metallicity. The fits are as follows:

$$GC: \frac{\dot{M}}{M_\odot \, yr^{-1}} = 8.8^{+40}_{-7.3} \times 10^{-6} \left(\frac{L}{10^4 \, L_\odot}\right)^{0.6\pm0.1}$$

$$\times \left(\frac{P}{500\,d}\right)^{0.5\pm0.3} \left(\frac{r_{gd}}{200}\right)^{0.05\pm0.07}, \qquad (4)$$

$$GB: \frac{\dot{M}}{M_\odot \, yr^{-1}} = 1.1^{+8.8}_{-1.0} \times 10^{-4} \left(\frac{L}{10^4 \, L_\odot}\right)^{0.8\pm0.1}$$

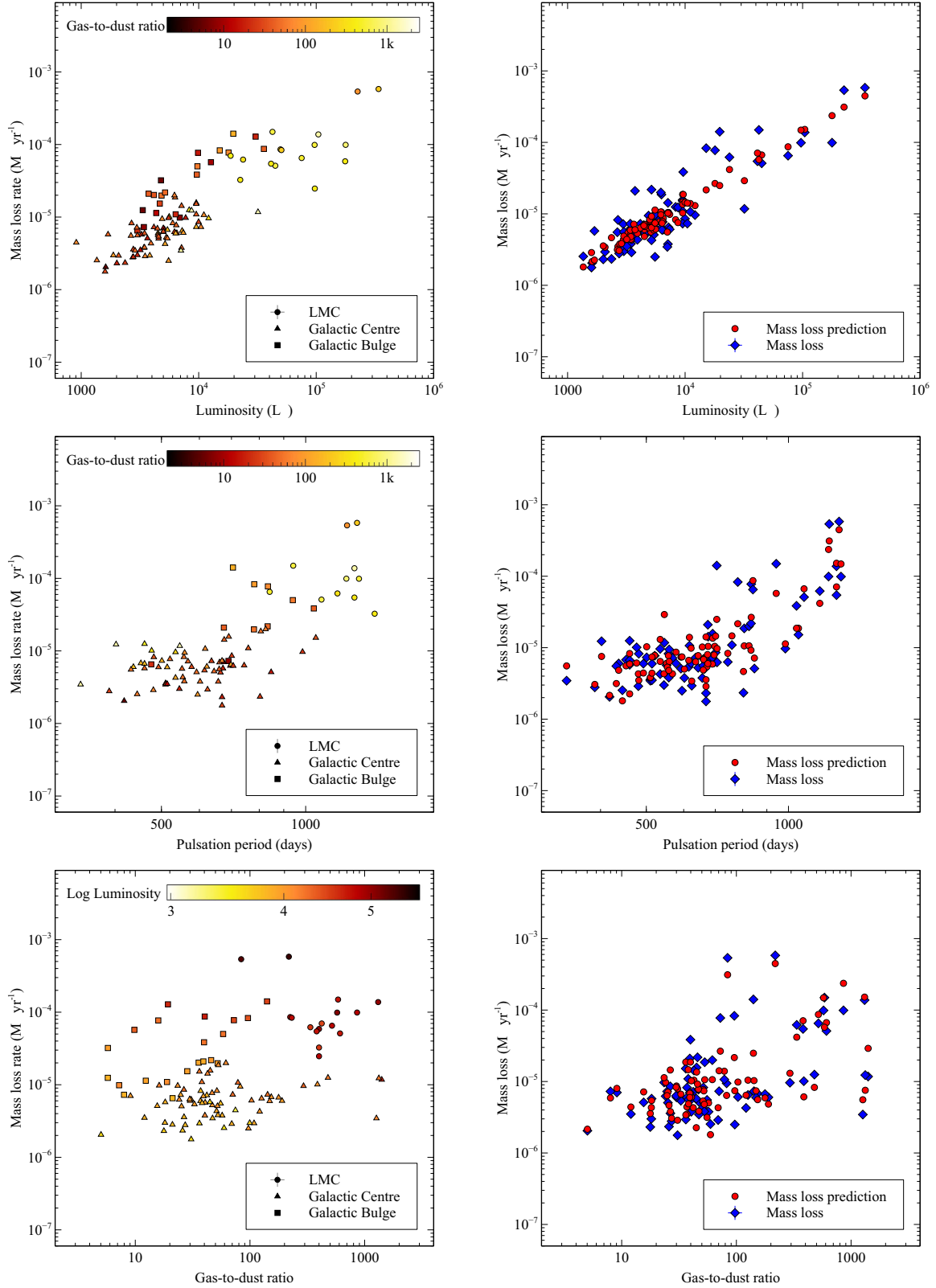$$\times \left(\frac{P}{500\,d}\right)^{-0.3\pm0.4} \left(\frac{r_{gd}}{200}\right)^{0.5\pm0.1}, \qquad (5)$$

$$LMC: \frac{\dot{M}}{M_\odot \, yr^{-1}} = 4.4^{+1226}_{-4.3} \times 10^{-5} \left(\frac{L}{10^4 \, L_\odot}\right)^{0.8\pm0.2}$$

$$\times \left(\frac{P}{500\,d}\right)^{-0.4\pm1.1} \left(\frac{r_{gd}}{200}\right)^{-0.4\pm0.2}. \qquad (6)$$

### 5.5 Interpretation of our prescription

Our mass-loss prescription, based entirely on observational data, matches known physical relationships. From the equation for optical depth (equation 1) from van Loon (2000), we know that

$$\tau(\lambda) \propto \frac{\dot{M}}{r_{gd} \, v_{exp} \sqrt{L}}, \qquad (7)$$

Figure 20. Mass-loss rate as a function of luminosity (top panels), pulsation period (middle panels), and gas-to-dust ratio (bottom panels). The left-hand column shows the observed mass-loss rates. The right-hand column shows the predicted mass-loss rates from our new mass-loss prescription (equation 3) plotted in red, with mass-loss rates derived by DUSTY for our sources with complete data (*L*, *P*, and r_{gd}) in blue. The missing sources in the top right-hand figure (as opposed to the left-hand figure) stem from a lack of pulsation period measurements in the Galactic bulge sample, which also correspond to the missing sources in the bottom right-hand figure.
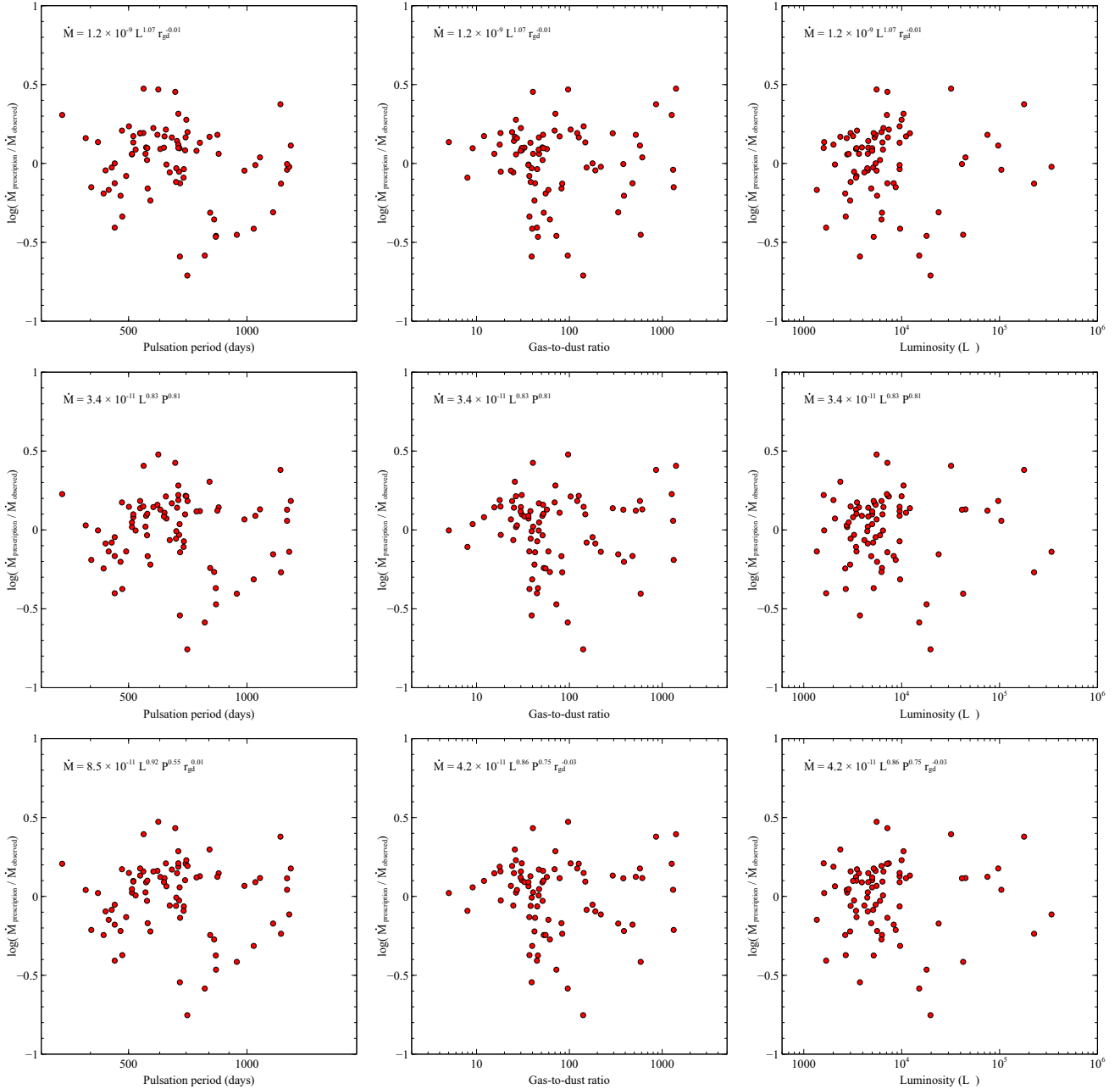
Figure 21. A comparison of mass-loss prescriptions. The *y*-axis in each figure is the log ratio of the prescription listed and the 'observed' mass-loss rates derived from DUSTY. In the top two rows are prescriptions which were fitted with only two parameters and in the bottom row is our mass-loss prescription which was fitted with all three. The two-parameter prescriptions show only a slightly larger deviation from the DUSTY mass-loss rates than our three-parameter prescription.

where τ is the optical depth. From our new relation for the expansion velocity (equation 2) shown in Fig. 17, we find that $v_{\rm exp} \propto ZL^{0.4}$. By combining these two, we get $\dot{M} \propto L^{0.9}\tau(\lambda)Zr_{\rm gd}$. As metallicity has been shown to be inversely proportional to the gas-to-dust ratio (van Loon 2000), and τ is a measure of the amount of photon scattering, all that remains is $\dot{M} \propto L^{0.9}$, which is exactly what we derive with our mass-loss prescription.

The second term in our prescription is pulsation period. If we describe the pulsation as a harmonic oscillation where gravity, g, is the driving force, then we expect that $2\pi/P \sim 1/t_{\rm freefall} \sim \sqrt{g(R)/R}$,

where R is the stellar radius. Based on the results from Schröder & Cuntz (2007), we find that $\dot{M} \propto 1/g$ (Fig. 22). This suggests that $\dot{M} \propto P^2/R$. Describing the star as a polytrope, with $MR^3 =$ constant, we expect $P \propto \sqrt{R/g} \propto M^{-1/2}R^{3/2} = R^3$, and hence, $\dot{M} \propto P^{5/3}$. This is a much stronger dependence on pulsation period than our prescription, $\dot{M} \propto P^{0.75}$; however, it includes the way mass-loss would increase as a result of the star being more luminous, hence larger and thus pulsating with a longer period (Fig. 23). At a given stellar effective temperature, $L \propto R^2$, which would suggest $L \propto P^{2/3}$. In our prescription, we find $\dot{M} \propto L^{0.9}P^{0.75}$. This
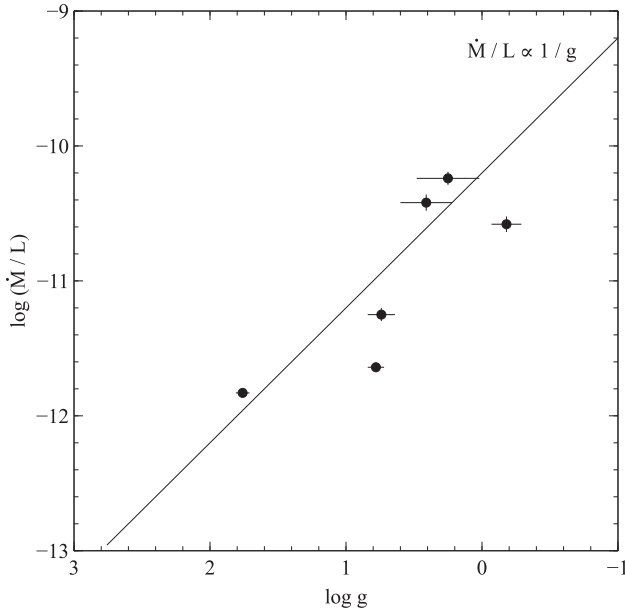
Figure 22. A comparison of the values of mass-loss and gravity (*g*) from the RSG sample from Schröder & Cuntz (2007). Their mass-loss rates have been divided by their derived luminosities, which, as we have shown (equation 3), should be approximately proportional to each other for a given value of gravity. This is done to isolate the dependence of mass-loss rate on gravity.
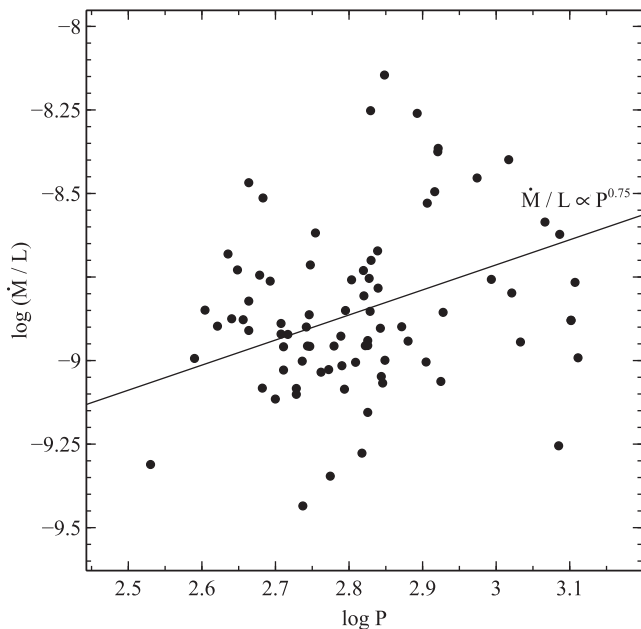
Figure 23. A comparison of mass-loss rate against pulsation period. We have again plotted the mass-loss rates divided by their derived luminosities to isolate the dependence of mass-loss rate on pulsation period.

would then suggest that our prescription has a total dependence on pulsation period according to $\dot{M} \propto P^{1.35}$. This brings it in closer (albeit not perfect) agreement with the above, simplistic expectation.

Fox & Wood (1982) and Wood (1990) calculated more sophisticated models for pulsating red giants and found that $P \propto R^{1.8}$

(with some dependence on mass). Replacing the above polytrope by this relationship would yield $\dot{M} \propto P^{1.44}$, which is in remarkable agreement with our empirical relationship.

The last term in our prescription is the gas-to-dust ratio. The gas-to-dust ratio has been shown to inversely scale with the metal content. Past studies have shown that metallicity has little to no effect on the mass-loss rates within Galactic and Magellanic Cloud AGB and RSG stars (van Loon 2000; van Loon et al. 2005). Our relation of $\dot{M} \propto r_{\rm gd}^{-0.03\pm0.07}$ matches this expectation and thus we can conclude that the gas-to-dust ratio has little effect on the mass-loss of AGB stars and RSGs within our Galaxy and the LMC. Though the wind is, the mass-loss itself does not appear to be driven by dust; the mass-loss rate is probably set by pulsation and/or other physical mechanisms originating in the stellar photosphere.

Our new mass-loss prescription uses three stellar parameters as gauges of physical differences within the sample. In general, we expect luminosity to give us the initial mass, gas-to-dust ratio to give us the metallicity, and pulsation period to give us the precise evolutionary stage within the superwind phase. We expect all three parameters to affect all of these physical differences to some degree.

5.6 Comparison to previous prescriptions

Most mass-loss prescriptions of AGB and RSG stars typically focus on specific stages of mass-loss and are derived using observational data. Past mass-loss prescriptions like the Reimers law (Reimers 1975), and the updated Reimers law (Schröder & Cuntz 2005), are used to calculate the mass-loss rates in the pre-dust-driven wind phase. These are based on the mass-loss of red giant branch stars and use luminosity, stellar radius, and mass; the updated prescription also uses effective temperature and gravity. Other prescriptions like that of van Loon et al. (2005) focus on mass-loss within the superwind phase and are based on the SED modelling of oxygen-rich AGB and RSG stars within the LMC. In-depth comparisons of previous mass-loss prescriptions have been done by Mauron & Josselin (2011) and Rosenfield et al. (2014).

We have compared our values for expansion velocities and mass-loss rates, computed by DUSTY, with the Galactic RSG sample from Mauron & Josselin (2011), as shown in Fig. 24. The Galactic RSGs are expected to have gas-to-dust ratio ~ 500 and fit well between our Galactic and LMC samples. Mass-loss rates were derived primarily by modelling the wind speeds from CO emission. This excludes the mass-loss rates of α Sco, derived by modelling the H II region (Reimers et al. 2008), of α Ori, derived by fitting C I lines (Huggins et al. 1994), and of VY CMa and μ Cep, derived by fitting the SEDs with DUSTY models (Shenoy et al. 2016). As these were derived using various methods and making different assumptions, we use caution in comparing them individually. We will, however, use the sample to understand how red supergiants fit within our more general picture of mass-loss in evolved stars. We have also displayed the calculated Galactic RSG mass-loss rates derived using our prescription (Fig. 24), in which we assume a gas-to-dust ratio of 500 and use pulsation periods from Kiss et al. (2006).

The literature values for mass-loss, which again use different methods of deriving the wind speeds and mass-loss rates, are generally much lower than our values for the mass-loss rates and we have plotted them in Fig. 24. Along with more accurate distances for our Galactic sources, and thus luminosities and mass-loss rates, new data have allowed for a more accurate measure of the optical depth. More accurate *Spitzer* data have allowed for a better
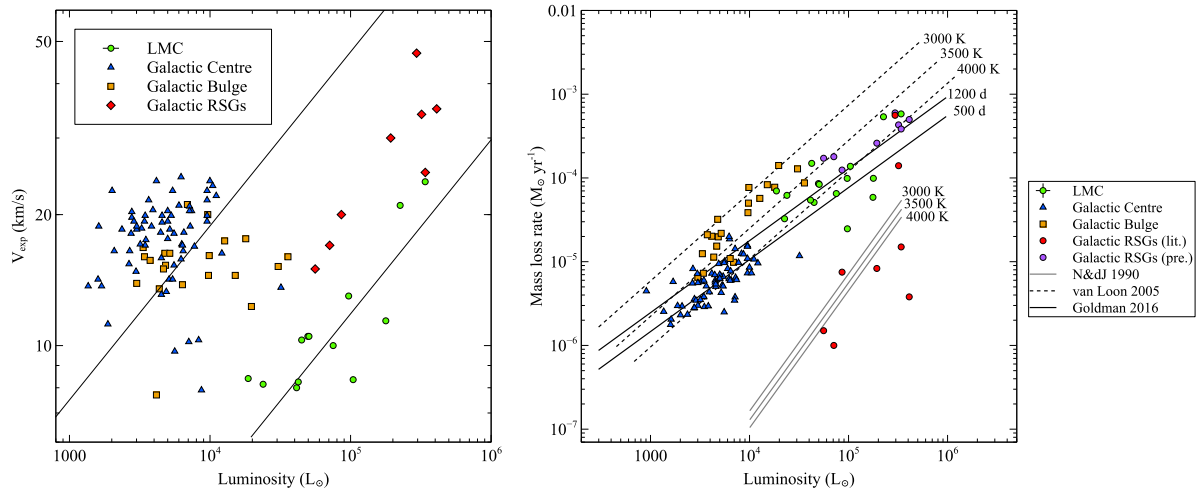
Figure 24. The observed wind speed as a function of luminosity (left-hand panel) and mass-loss rates as a function of luminosity (right-hand panel), as shown in Figs 16 and 19, with the Galactic RSG sample from Mauron & Josselin (2011); we have used updated literature mass-loss rates for VY CMa and μ Cep from Shenoy et al. (2016). We show literature mass-loss values (Galactic RSGs lit.) and the calculated mass-loss rates (assuming an $r_{gd} = 500$) using our mass-loss prescription (Galactic RSGs pre.) and the pulsation periods from Kiss et al. (2006); NML Cyg pulsation period is from Monnier et al. (1997). Also plotted are the mass-loss prescriptions by Nieuwenhuijzen & de Jager (1990) and van Loon et al. (2005), as well as our own (Goldman 2016), with a range of values for unknown variables (either effective temperature or pulsation period).

measure of IR excesses as well as a decrease of confusion from contaminating sources within the observing fields. We have also compared our mass-loss prescription with previous mass-loss prescriptions (Fig. 24), plotting different values for unknown variables (either effective temperature, expansion velocity, or pulsation period). The comparison suggests that some of the sources within the Galactic RSG sample may not be within the superwind phase of mass-loss. We will discuss the evolutionary stages of these sources further in the following section.

5.7 Fundamental stellar parameters and mass-loss

Our current analysis covers highly evolved AGB and RSG stars with a luminosity range from 2000 to over 300 000 $L_\odot$ and a metallicity range of a half to twice solar. This range allows us to draw conclusions about the mass-loss mechanism and how it is affected by fundamental differences within the stars. We expect L, r_{gd}, and P to relate to mass, metallicity, and evolutionary phase. While the links between luminosity and initial mass, and r_{gd} and metallicity are more established (e.g. Vassiliadis & Wood 1993; Blöcker 1995), evidence for a link between pulsation period and evolutionary stage is still unclear (Groenewegen et al. 2007; Sloan et al. 2012). As our stars progress through the superwind stage, stellar pulsation will become stronger and slower. We expect that this pulsation period may be able to give us an indication of the source's stage within the superwind phase. We will discuss each of these relationships in the following subsections.

Mass (initial and current). The initial mass will have a dramatic impact on the evolution of these stars. Dredge-up efficiency and hot-bottom burning will vary with initial mass; thus, the C/O ratio of these stars will depend on the initial mass (e.g. Boothroyd et al. 1995; Karakas 2010). In terms of mass-loss, a higher initial mass will allow the star to get to a higher luminosity before the onset of the superwind phase, thus resulting in a higher mass-loss rate. As these sources reach more advanced stages within the superwind phase, their mass will decrease as their luminosity remains the same. We expect that a higher luminosity will result in a higher mass-loss rate. In these stars, we know that the dust-formation zone will depend on luminosity, being farther away for more massive

stars. Looking at the ratio of luminosity and current mass (L/M), our higher luminosity RSGs ($\sim$200 000 $L_\odot$) and lower luminosity sources ($\sim$50 000 $L_\odot$) have masses of around 20 and 5 $M_\odot$, respectively, and quite similar L/M ratios. Assuming this ratio to be constant within our samples, we expect the ratio of radiation flux and gravity to be independent of radius as both depend on radial distance as r^{-2}. The acceleration is determined by the *difference* between the radiation pressure and gravity, which, at any given radius, is larger for more massive (more luminous) stars with the same L/M ratio. However, the wind – and ultimately the mass that is lost – is driven by dust grains, which condense at a distance where the dust grain equilibrium temperature matches the condensation temperature. This happens at a certain photon flux, i.e. farther from a more luminous star by a factor of $R^2 \equiv L$, thus balancing out the larger difference between radiation pressure and gravity at a given distance. But because the area through which the mass flows also increases in proportion to R^2, the total amount of mass flowing through the area increases accordingly, and thus, $\dot{M} \propto L$.

As these sources lose mass in the superwind phase and remain at a constant luminosity, L/M will increase, making it easier to drive the wind, whereas the decrease in mass will drive a direct increase in P. The source will then evolve to longer pulsation periods at a constant luminosity; we expect that this is the case for our extreme Galactic bulge sample. It is still unclear whether the simultaneous increase in pulsation period affects the mass-loss. With longer and larger pulsations, as well as reduced gravity at the surface of a larger star which has lost mass, this should allow stars to levitate more material out to form dust and more easily drive mass-loss. We expect L/M to affect the mass-loss rate directly, and indirectly through changes in the pulsation period. However, we are not at a stage where we can fully quantify these relationship.

Metallicity. Gas-to-dust ratios have been shown to scale inversely proportionally with metallicity (van Loon 2000), and thus, we can use them to understand the effects of metallicity. Metallicity will have a dramatic impact on the dust production of oxygen-rich AGB and RSG stars as well as the chemical composition of the dust itself (Jones 2013). Unlike carbon stars, these stars cannot create the raw materials for dust production. Past studies have shown that while nearby Galactic and Magellanic Cloud oxygen-rich stars have

similar total mass-loss rates at higher luminosities, the dust mass-loss rates show a strong dependence on metallicity (Wood et al. 1998; van Loon 2000; Lagadec et al. 2008); this is consistent with our results.

Observations of Galactic and Magellanic Cloud carbon AGB stars have been interpreted to show that the quantity of carbon dust produced in both environments is the same. It has also been suggested that LMC carbon stars collectively produce more dust than their oxygen-rich counterparts (Boyer et al. 2011; Matsuura 2013; Sloan et al. 2016). It was suggested by Habing (1996) that carbon-rich LMC AGB stars may have similar gas-to-dust ratios to those of Galactic samples. If this is the case, it also stands to reason that they will have expansion velocities comparable to those of the Galactic samples. However, van Loon et al. (2008) present evidence suggesting that the effect of primary carbon may not be as large, which would mean that also Magellanic carbon star winds are expected to be less dusty, and slower, than solar-metallicity carbon stars.

It was predicted that AGB mass-loss would be dependent on metallicity as an increase in dust optical depth may cause an increase in the number of absorbing and scattering events of photons on dust grains, and therefore an increase in the net driving force of the dust-driven wind (Gail & Sedlmayr 1986). While the dust content and driving of the wind depend on metallicity, we see no evidence to suggest a metallicity dependence on the mass-loss. We expect that at lower metallicities, the mass is lost in a slower denser outflow with the same net mass-loss efficiency.

Evolutionary phase. As our sources become more evolved and more extreme, the strength and cycle length of stellar pulsations will increase. In theory, we can use the pulsation period at a given luminosity as a gauge of the stage within the superwind phase. As mass decreases due to mass-loss, the pulsation period increases, and reduced gravity at the surface leads to increased mass-loss. We know that as the mass-loss ramps up, the gas-to-dust ratio will also change. As the mass-loss in our sources has been found to be insensitive to metallicity, this implies that we are looking at sources in the superwind phase where they have reached maximal dust formation efficiency.

Stellar pulsations can be affected by chemical differences in the star. The pulsation amplitude of oxygen-rich AGB stars may be affected by metallicity as TiO absorption is affected by metallicity, but it is unclear if the pulsation period will be affected by changes in metallicity as it is determined deeper inside the star. The efficiency of the dust formation will also vary with evolutionary phase, which may leave some evolved stars like Betelgeuse with little dust (van Loon 2013). However, this source has not entered its superwind phase and would be incompatible with our mass-loss prescription.

In this work, we have fitted a mass-loss prescription using several stellar samples selected in the superwind stage of mass-loss. We have also included the Galactic RSG sample for comparison as these sources seem to follow a similar mass-loss mechanism. However, this sample contains sources not within the superwind phase, and our prescription may not be able to provide a realistic estimation of the mass-loss rate of these sources. In Fig. 24, we see that the Nieuwenhuijzen and de Jager prescription fits the bulk of the RSG sample much better. Two of these sources, VY CMa and NML Cyg with mass-loss rates of 5.4×10^{-5} and 1.4×10^{-5} $M_\odot$ yr^{-1}, respectively, fit well within our other samples. It is surprising that, given VY CMa shows silicate in emission rather than absorption (Harwit et al. 2001), this source would show such a high mass-loss rate compared to the rest of the sample. However, these sources are luminous and have the lowest effective temperatures of the RSG sample, may thus be comparable to our sample, whereas the remaining RSGs may be at an early evolutionary stage. A similar gap in mass-loss rates of LMC RSGs of the order of 2 mag has been found in the past by van Loon et al. (1999). It appears that at least within RSGs another parameter is affecting the mass-loss.

6 CONCLUSIONS

We present the results of our recent survey of 1612-MHz OH maser emission in the LMC. We have discovered four new sources and increased the number of reliable wind speeds from five to 13. The expansion velocities derived from our maser sources fit well with our updated relation for dust-driven winds. We have developed a method of deriving gas-to-dust ratios of OH/IR stars by modelling the SED and scaling the results with the expansion velocities derived from maser observations. Furthermore, we have used these new results to develop an empirical mass-loss prescription which includes the effects of metallicity and luminosity. The results show a correlation of mass-loss with pulsation period, with an even tighter correlation between mass-loss and luminosity. We see a clear link between expansion velocity and gas-to-dust ratio; yet, the gas-to-dust ratio has little effect on the mass-loss of AGB stars and RSGs. This suggests that mass-loss is (nearly) independent of metallicity between a half and twice solar.

REFERENCES

Baud B., Habing J. H., 1983, A&A, 127, 73
Beichman C. A., Neugebauer G., Habing H. J., Clegg P. E., Chester T. J., 1988, NASA Ref. Publ., 1190, 1
Blöcker T., 1995, A&A, 297, 727
Boothroyd A. et al., 1995, ApJ, 442, L21
Boyer M. L. et al., 2011, A&A, 142, 103
Buchanan C., Kastner J. H., Forrest W. J., Hrivnak B. J., Sahai R., Egan M., Frank A., Barnbaum C., 2006, AJ, 132, 1890
Bujarrabal V., Guibert J., Nguyen-Q-Rieu Omont A., 1980, A&A, 84, 311
Catchpole R. M., Whitelock P. A., Feast M. W., Hughes S. M. G., Irwin M., Alard C., 2016, MNRAS, 455, 2216
Choudhury S., Subramaniam A., Cole A., 2016, MNRAS, 455, 1855
Cioni M. R. et al., 2000, A&AS, 144, 235
Cohen R.J., Downs G., Emerson R., Grimm M., Gulkis S., Stevens G., Tarter J., 1987, MNRAS, 225, 491
Cutri R. M. et al., 2003, Vizier On-line Data Catalog, 2246, 0
Dickey J. M. et al., 2013, Publ. Astron. Soc. Aust., 30, 3

Dijkstra C., Speck A. K., Reid R. B., Abraham P, 2005, ApJ, 633, L133

Do T., Kerzendorf W., Winsor N., Støstad M., Morris M. R., Lu J. R., Ghez A. M., 2015, ApJ, 809, 143

Egan M. P., Price S. D., Kraemer K. E., 2003, BAAS, 35, 1301

Elitzur M., Goldreich P., Scoville N., 1976, ApJ, 205, 384

Elitzur M., 1992, Astronomical Masers. Kluwer, Dordrecht

Elitzur M., Ivezić Ž., 2001, MNRAS, 327, 403

Engels D., Bunzel F., 2015, A&A, 582, A68

Fazio G. G. et al., 2004, ApJS, 154, 10

Feast M. W., 2013, in Oswalt T. D., Gilmore G., eds, Planets, Stars and Stellar Systems Vol. 5, Galactic Distance Scales, Springer, Dordrecht, p. 829

Fox M. W., Wood P. R., 1982, ApJ, 259, 198

Gail H. P., Sedlmayr E., 1986, A&A, 161, 201

García-Hernández D. A. et al., 2009, ApJ, 705, L31

Groenewegen M. et al., 2007, MNRAS, 376, 313

Habing H. J., 1996, A&AR, 7, 97

Habing H. J., Tignon J., Tielens A. G. G. M., 1994, A&A, 286, 523

Harvey P. M., Bechis K. P., Wilson W. J., Ball J. A., 1974, ApJS, 27, 331

Harwit M., Malfait K., Decin L., Waelkens C., Feuchtgruber H., Melnick G. J., 2001, ApJ, 557, 844

Herwig I., 2005, ARA&A, 43, 435

Höfner et al., 2016, A&A, 594, 108

Huggins P. J., Bachiller R., Cox P., Forveille T., 1994, ApJ, 424, L127

Humphreys R. M., 1978, ApJS, 38, 309

Humphreys R. M., Davidson K., Ruch G., Wallerstein G., 2005, AJ, 129, 492

Humphreys R. M., Helton L. A., Jones T. J., 2007, AJ, 133, 2716

Iben I., Jr, Renzini A., 1983, ARA&A, 21, 271

Imai H., Katayama Y., Ellingsen S. P., Hagiwara Y., 2013, MNRAS, 432, L16

Jiménez-Esteban F. M., Engels D., 2015, A&A, 579, A76

Jones O., 2013, PhD thesis, Univ. Manchester

Jones O. et al., 2012, MNRAS, 427, 3209

Jones O. C., Meixner M., Sargent B. A., Boyer M. L., Sewiło M., Hony S., Roman-Duval J., 2015, ApJ, 811, 145

Karakas A. I., 2010, MNRAS 403, 1413

Kemper F. et al., 2010, PASP, 122, 683

Kim D.-W., Protopapas P., Bailer-Jones C. A. L., Byun Y.-I., Chang S.-W., Marquette J.-B., Shin M.-S., 2014, A&A, 566, 43

Kiss L. L., Szabó Gy. M., Bedding T. R., 2006, MNRAS, 372, 1721

Lagadec E. et al., 2008, MNRAS, 390, L59

Lebouteiller V., Barry D. J., Spoon H. W. W., Bernard-Salas J., Sloan G. C., Houck J. R., Weedman D. W., 2011, ApJS, 196, 8

Levesque E. M., Massey P., Plez B., Olsen K. A. G., 2009, AJ, 137, 4744

Lindqvist M., Winnberg A., Habing H. J., Matthews H. E., 1992, A&AS, 92, 43

McMullin J. P., Waters B., Schiebel D., Young W., Golap K., 2007, in Shaw R. A., Hill F., Bell D. J., eds, ASP Conf. Ser. Vol. 376, Astronomical Data Analysis Software and Systems XVI. Astron. Soc. Pac., San Francisco, p. 127

Marshall J. R., van Loon J. Th., Matsuura M., Wood P. R., Zijlstra A. A., Whitelock P. A., 2004, MNRAS, 355, 1348

Mathis J. S., Rumpl W., Nordsieck K. H., 1977, ApJ, 217, 425

Matsuura M., 2013, MNRAS, 429, 2527

Mauron N., Josselin E., 2011, A&A, 526, 156

Meixner M. et al., 2006, AJ, 132, 2268

Meixner M. et al., 2013, AJ, 146, 62

Minniti D. et al., 2010, New Astron., 15, 433

Monnier J. D. et al., 1997, ApJ, 481, 420

Nataf et al., 2016, MNRAS, 456, 2692

Nieuwenhuijzen H., de Jager C., 1990, A&A, 231, 134

Nyman L.-Å., Hall P. J., Olofsson H., 1998, A&AS, 127, 185

Ohnaka K., Driebe T., Hofmann K.-H., Weigelt G., Wittkowski M., 2008, A&A, 484, 371

Olsen K. A. G., Zaritsky D., Blum R. D., Boyer M. L., Gordon K. D., 2011, A&A, 737, 29

Ossenkopf V., Henning Th., Mathis J. S., 1992, A&A, 261, 567

Pierce M. J., Jurcevic J. S., Crabtree D., 2000, 313, 271

Ramstedt S., Schöier F. L., Olofsson H., Lundgren A. A., 2008, A&A, 487, 645

Reimers D., 1975, Mem. Soc. R. Sci. Liège, 8, 369

Reimers D., Hagen H.-J., Baade R., Braun K., 2008, A&A, 491, 229

Richards A. M. S., Yates J. A., 1998, Irish Astron. J., 25, 7

Richards A. M. S. et al., 2014, A&A, 572, L9

Riebel D., Srinivasan S., Sargent B., Meixner M., 2012, ApJ, 753, 71

Riebel D. et al., 2015, ApJ, 807, 1

Rieke G. H., Lebofsky M. J., 1985, ApJ, 288, 618

Rieke G. H. et al., 2004, ApJS, 154, 25

Roche P. F., Aitken A. K., Smith C. H., 1993, MNRAS, 262, 301

Roman-Duval J. et al., 2014, ApJ, 797, 86

Rosenfield P. et al., 2014, ApJ, 790, 22

Sargent B. A., Srinivasan S., Meixner M., 2011, ApJ, 728, 93

Sault R. J., Teuben P. J., Wright M. C. H., 1995, in Shaw R. A., Payne H. E., Hayes J. J. E., eds, ASP Conf. Ser. Vol. 77, Astronomical Data Analysis Software and Systems IV. Astron. Soc. Pac., San Francisco, p. 433

Schröder K., Cuntz M., 2005, ApJ, 630, L73

Schröder K. P., Cuntz M., 2007, A&A, 465, 593

Schultheis M. et al., 2014, A&A, 566, A120

Shenoy D. et al., 2016, ApJ, 151, 51

Sloan G., Kraemer K. E., Wood P. R., Zijlstra A. A., Bernard-Salas J., Devost D., Houck J. R., 2008, ApJ, 686, 1056

Sloan G. et al., 2012, ApJ, 752, 140

Sloan G. et al., 2016, ApJ, 826, 44

Staveley-Smith L., Kim S., Calabretta M. R., Haynes R. F., Kesteven M. J., 2003, MNRAS, 339, 87

te Lintel Hekkert P., Caswell J. L., Habing H. J., Haynes R. F., Norris R. P., 1991, A&AS, 90, 327

Trams N. R. et al., 1999, A&A, 346, 843

van Aarle E., van Winckel H., Lloyd Evans T., Ueta T., Wood P. R., Ginsburg A. G., 2011, A&A, 530, A90

van der Veen W. E. C. J., Habing H. J., 1990, A&A, 231, 404

van Loon J. Th., 2000, A&A, 354, 125

van Loon J. Th., 2012, in Braun R., ed., Science with Parkes 50 Years Young, preprint (arXiv:1210.0983)

van Loon J. Th., 2013, EAS Publ. Ser., 60, 307

van Loon J. Th., Zijlstra A. A., Bujarrabal V., Nyman L.-Å., 1996, A&A, 306, L29

van Loon J. Th., Zijlstra A. A., Whitelock P. A., Waters L. B. F. M., Loup C., Trams N. R., 1997, A&A, 325, 585

van Loon J. Th. et al., 1998a, A&A, 329, 169

van Loon J. Th., te Lintel Hekkert P., Bujarrabal V., Zijlstra A. A., Nyman L.-Å., 1998b, A&A 337, 141

van Loon J. Th., Groenewegen M. A. T., de Koter A., Trams N. R., Waters L. B. F. M., Zijlstra A. A., Whitelock P. A., Loup C., 1999, A&A, 351, 559

van Loon J. Th., Zijlstra A. A., Kaper L., Gilmore G. F., Loup C., Blommaert J. A. D. L., 2001a, A&A 368, 239

van Loon J. Th., Zijlstra A. A., Bujarrabal V., Nyman L.-Å., 2001b, A&A, 368, 950

van Loon J. Th., Marshall J. R., Zijlstra A. A., 2005, A&A, 438, 273

van Loon J. Th., Cohen M., Oliveira J. M., Matsuura M., McDonald I., Sloan G. C., Wood P. R., Zijlstra A. A., 2008, A&A, 487, 1055

Vassiliadis E., Wood P. R., 1993, ApJ, 413, 641

Verhoelst T., van der Zypen N., Hony S., Decin L., Cami J., Eriksson K., 2009, A&A, 498, 127

Werner M. W. et al., 2004, ApJS, 154, 1

Whitelock P. A. et al., 1991, MNRAS, 248, 276

Whitelock P. A., Feast M. W., van Loon J. Th., Zijlstra A. A., 2003, MNRAS, 342, 86

Whiting M., 2012, ApJ, 421, 3242

Wood P. R., 1990, in Cacciari C., Clementini G., eds, ASP Conf. Ser. Vol. 11, Confrontation Between Stellar Pulsation and Evolution. Astron. Soc. Pac., San Francisco, p. 355

Wood P. R., Bessel M. S., Whiteoak J. B., 1986, ApJ, 306, L81

Wood P. R., Whiteoak J. B., Hughes S. M. G., Bessell M. S., Gardner F. F., Hyland A. R., 1992, ApJ, 397, 552

Wood P. R., Habing H. J., McGregor P. J., 1998, A&A, 336, 925

Woods P. M. et al., 2011, MNRAS, 411, 1597
Xue M., Jiang B. W., Gao J., Liu J., Wang S., Li A., 2016, ApJS, 224, 23
Yamamura I., Makiuti S., Ikeda N., Fukuda Y., Oyabu S., Koga T., White G. J., 2010, VizieR On-line Data Catalog, 2298, 0

Zijlstra A. A., Loup C., Waters L. B. F. M., Whitelock P. A., van Loon J. Th., Guglielmo F., 1996, MNRAS, 279, 32
Zoccali M. et al., 2003, A&A, 399, 931

APPENDIX A: SED MODELLING OF GALACTIC SOURCES

We have modelled a number of Galactic sources from the Lindqvist et al. (1992) Galactic Centre sample of OH/IR stars and the Jiménez-Esteban & Engels (2015) Galactic bulge sample of more extreme OH/IR stars. Using the same approach as in our LMC sample, we have fitted 69 Galactic Centre and 21 Galactic bulge OH/IR stars with DUSTY models. These samples serve as a comparison sample at higher metallicity.
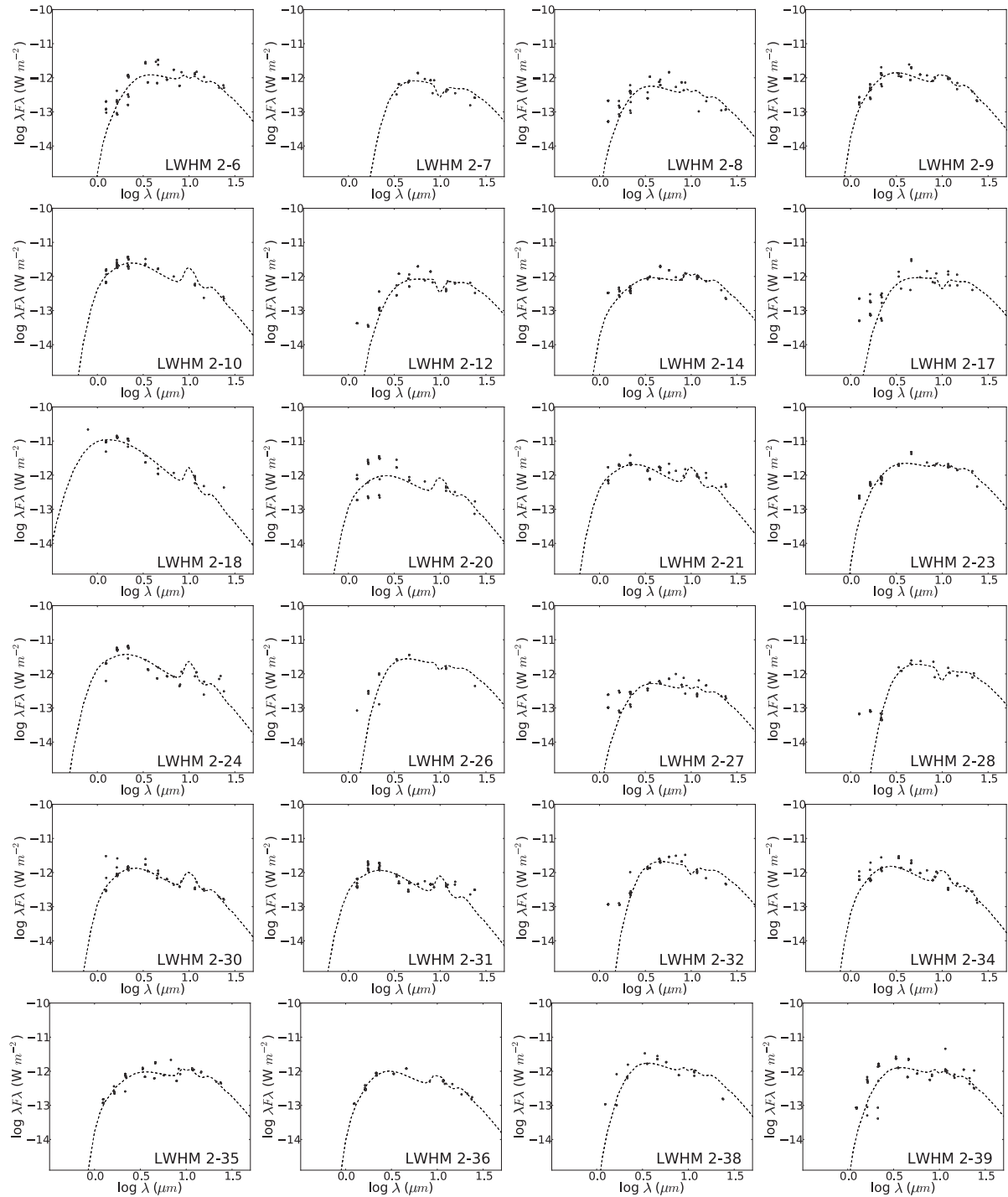
Figure A1. SED fitting of DUSTY models to the dereddened photometry from our Galactic Centre sources.
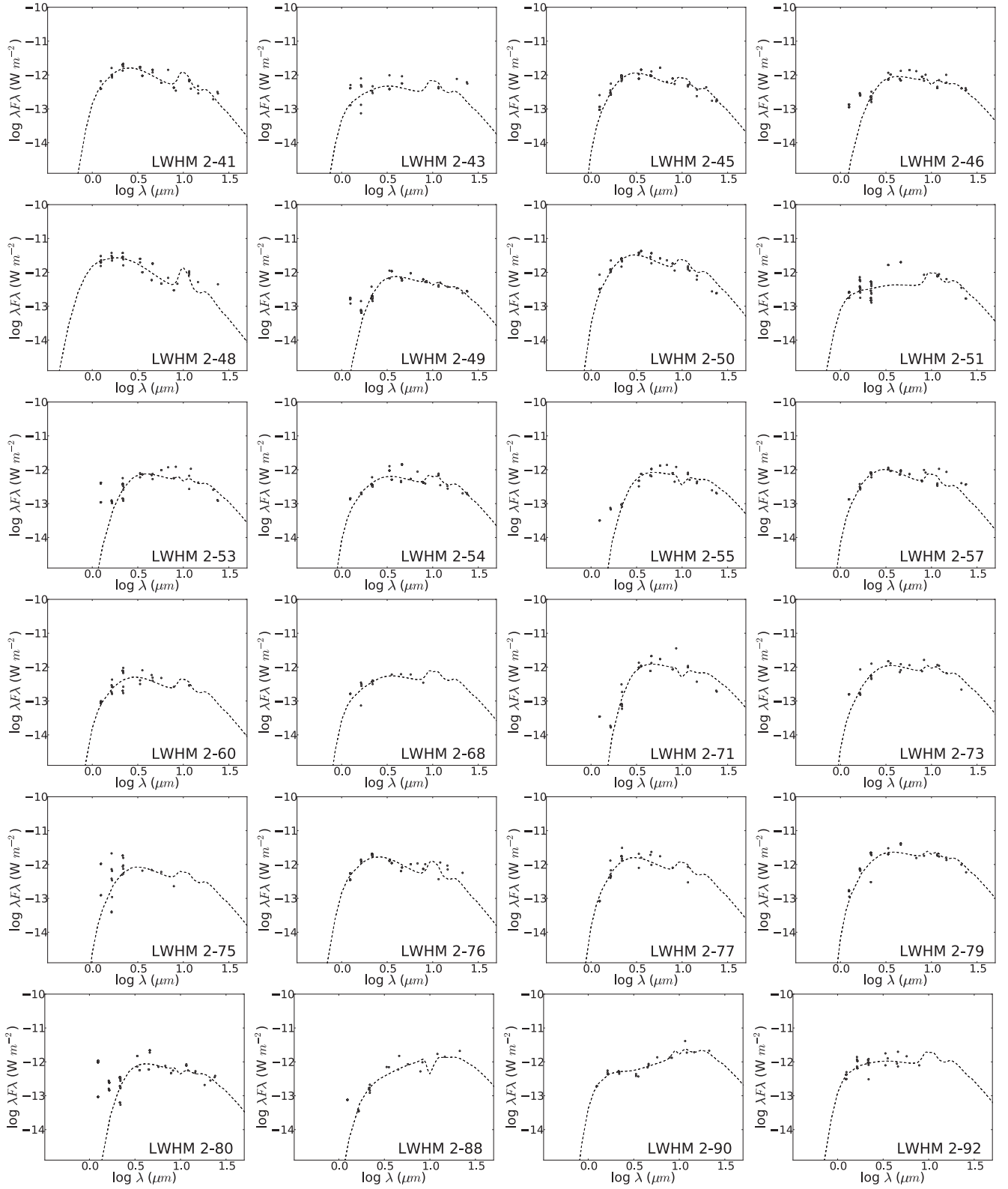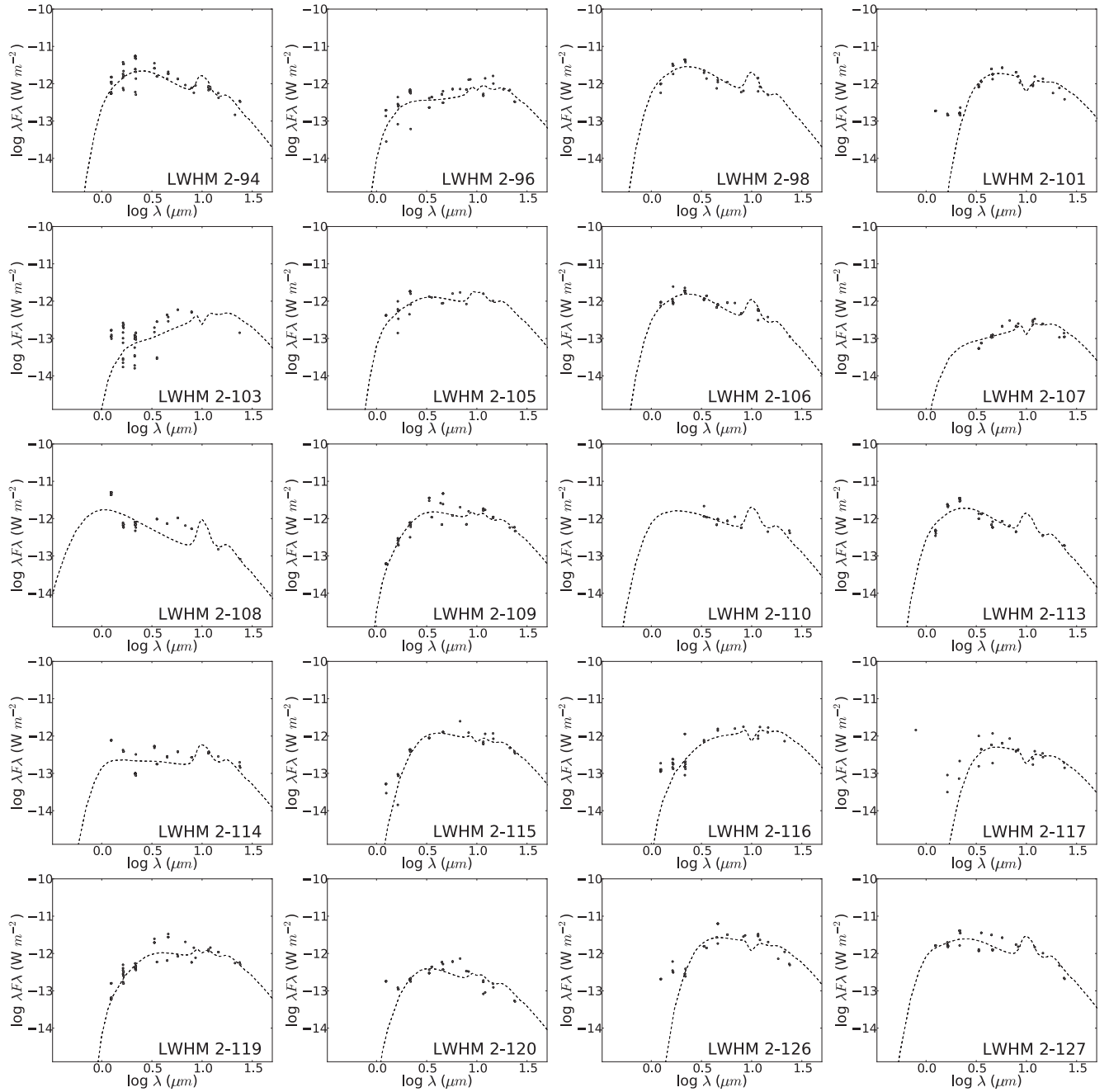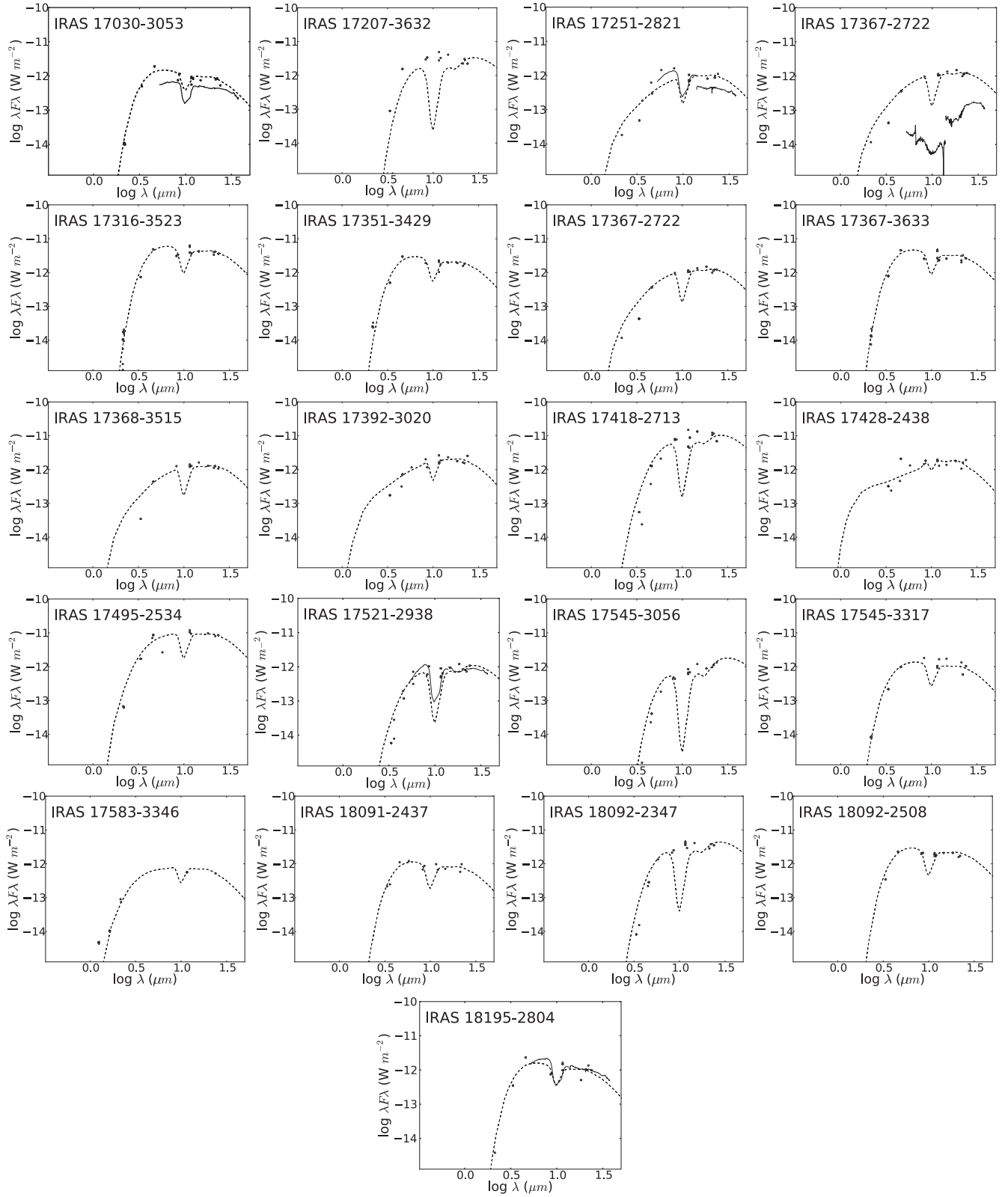
Figure A1 – *continued*

Figure A1 – *continued*

Figure A2. SED fitting of DUSTY models to the dereddened photometry from our Galactic bulge sources.

APPENDIX B: GALACTIC OH MASER SOURCES

We observed eight Galactic maser sources with Parkes, in addition to our LMC sources, for pointing checks (Table B1). We did not find any noticeable changes in expansion velocity when compared with previous observations, but we did identify several interesting features. From the observation of IRAS 18139−1816, we found an absorption feature around 30 km s^{-1}. We expect that this is a result of absorption within the nearby dust cloud, which can be seen in optical images of the region. We also found a secondary maser source during our observation of IRAS 18268−1117. This additional maser profile is coming from another source within the 13-arcmin beam of Parkes. The only potential known sources within around 13 arcmin are the evolved S-type AGB star, IRAS 18269−1111, and the source IRAS 18272−1117. The S-type source has a carbon-to-oxygen ratio of 1, making it an unlikely candidate for OH maser emission but still within the realm of possibility, especially if it has recently undergone an additional thermal pulse and the OH shell corresponds to a time when it was still an M giant.

**Table B1.** Results of Galactic maser observations.

Object name	Alternative name	l (°)	b (°)	v_{exp} (km s^{-1})	F_{25} (Jy)	F_{int} (Jy km s^{-1})		Velocity at peaks (km s^{-1})	
						(red)	(blue)	(red)	(blue)
IRAS 18115−2139	OH 9.575 −2.032	9.574	−2.031	14.2	60.8	8.85	7.47	−18.4	10.0
IRAS 18139−1816	OH 12.8 −0.9	12.819	−0.901	12.1	16.9	9.21	11.22	−81.1	−56.8
IRAS 18257−1000	OH 21.5 +0.5	21.451	+0.500	18.4	120.5	39.7	30.3	82.4	119.1
IRAS 18268−1117	OH 20.4 −0.3	20.433	−0.344	17.4	30.5	6.15	9.22	9.6	44.4
IRAS 18268−1117 B				16.4		0.82	0.58	78.6	111.4
IRAS 18432−0149	OH 30.7 +0.4	30.715	+0.423	17.5	52.3	15.7	12.5	32.3	67.3
IRAS 18460−0254	OH 30.09 −0.69	30.086	−0.681	20.3	279.9	116.4	131.2	62.1	102.7
IRAS 19059−2219	V* V3880 Sgr	14.662	−13.610	13.0	211.6	8.23	4.5	−3.0	23.0
IRAS 20077−0625	V* V1300 Aql	36.356	−20.415	12.6	1061.0	18.9	8.46	−44.9	−19.8
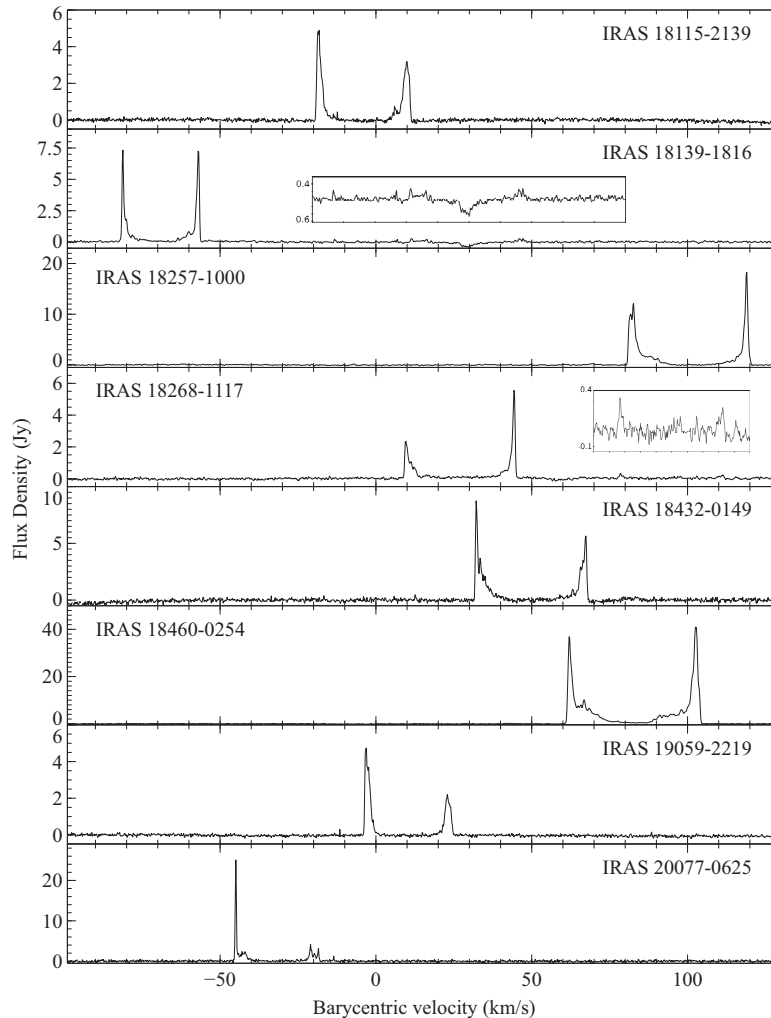
Figure B1. OH 1612-MHz maser emission from our Parkes observations of additional Galactic sources. Sources are from different Galactic samples from those modelled in previous sections.

APPENDIX C: UVES SPECTRA

We have been able to determine systemic velocities for two of our LMC sources, IRAS 04407−7000 and IRAS 04516−6902, using UVES-reduced spectra from the ESO data archive. Using a cross-spectrum fitting technique, we have fitted the molecular bandheads of these two sources to that of the UVES spectrum of IRAS 04498−6842. This technique has allowed us to determine the best-fitting phase difference and the velocity shift. We have used the bright source IRAS 04498−6842 as our model, which has a clear maser profile yielding a systemic velocity of 260 km s^{-1}. The systemic velocities for IRAS 04407−7000 and IRAS 04516−6902 seem to fit well between the maser profiles, corroborating the weaker maser peaks and providing more evidence for all three maser profiles.
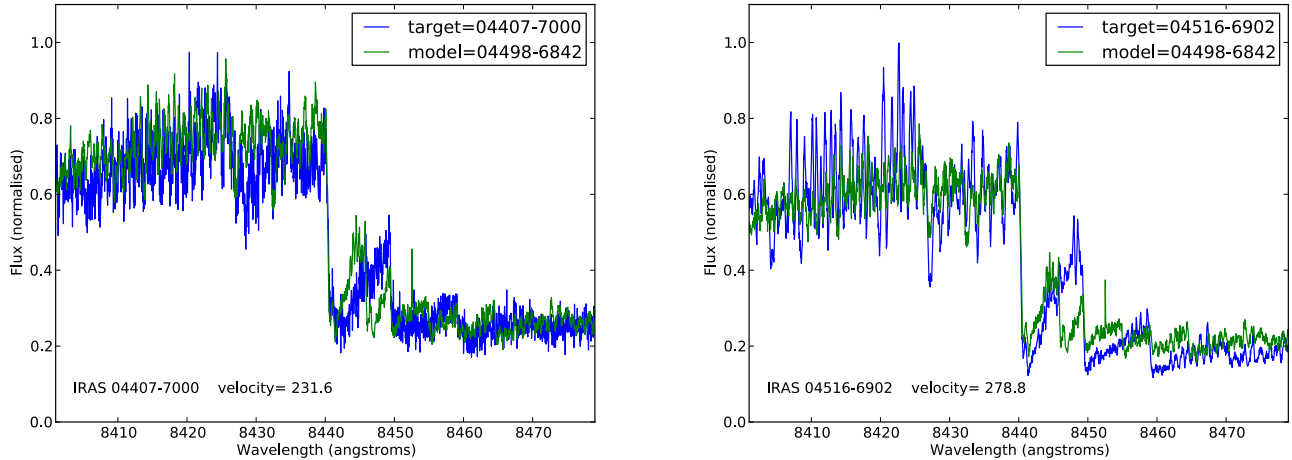
Figure C1. UVES spectra of IRAS 04407−7000 and IRAS 04516−6902 fitted with the UVES spectrum of IRAS 04498−6842 using a cross-spectrum fitting technique. The phase shift has been used to calculate systemic velocities for these sources.

APPENDIX D: VVV PULSATION PERIODS

We have derived pulsation periods for seven Galactic bulge stars from the Jiménez-Esteban & Engels (2015) Galactic bulge sample of extreme highly reddened OH/IR stars. Aperture photometry was done on *K*-band photometry for all of our Galactic bulge sources within the tiles of the VVV survey (Minniti et al. 2010). A calibrator star was used in each field to derive the relative flux. Fourier analysis was used to fit the period and a least-squares fit was used to calculate the errors. Three of the sources have previously derived pulsation periods from van der Veen & Habing (1990). Our periods of 690, 781, and 833 d are dramatically different from the values previously derived of 1200, 1500, and 1200, respectively. The inaccuracy of these derived periods has been shown in Whitelock et al. (1991) and now in this work.
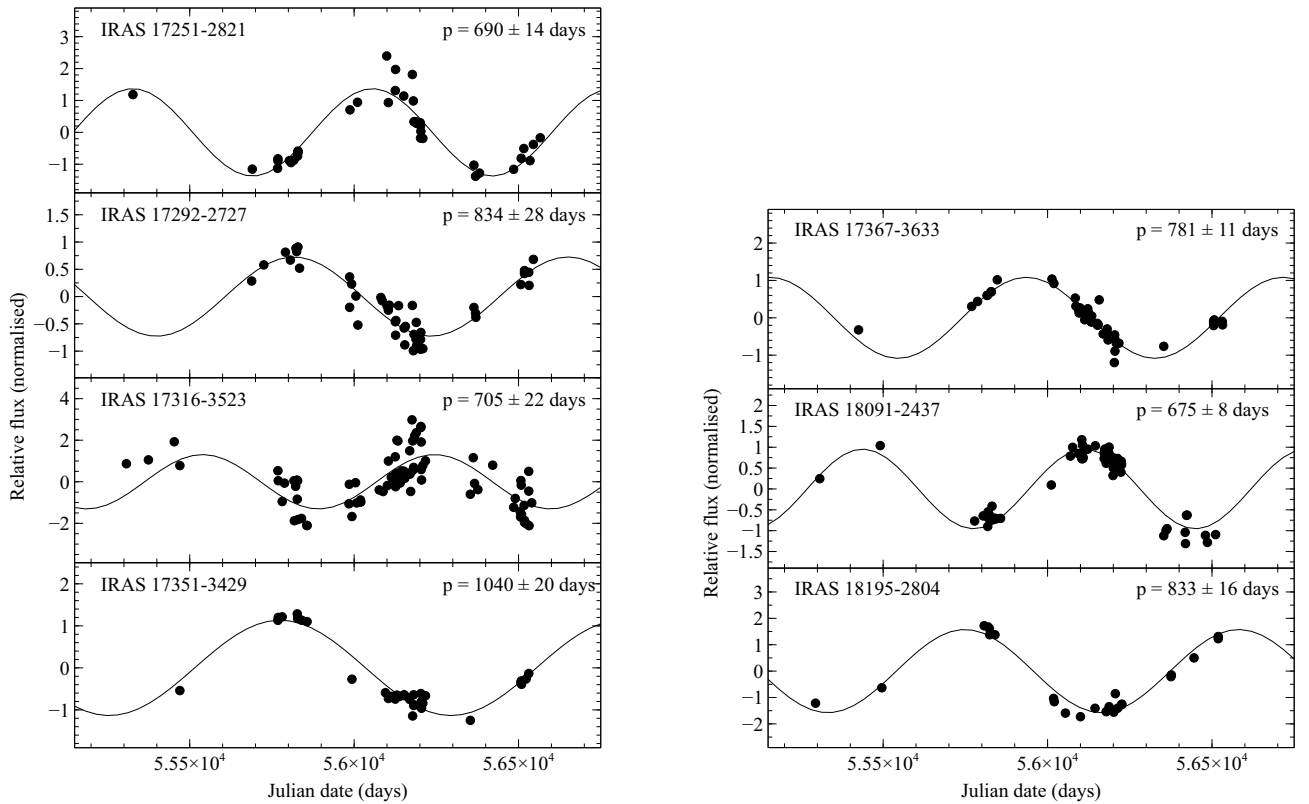
Figure D1. Fit pulsation periods of highly evolved stars from our Galactic bulge sample. Aperture photometry was done on tiles from the VVV survey and fitted using a Fourier analysis fitting technique.

This paper has been typeset from a TₑX/LAᵀₑX file prepared by the author.